

WiSE-OD: Benchmarking Robustness in Infrared Object Detection

Heitor R. Medeiros Atif Belal Masih Aminbeidokhti
Eric Granger Marco Pedersoli
LIVIA, Dept. of Systems Engineering, ETS Montreal, Canada
International Laboratory on Learning Systems (ILLS)

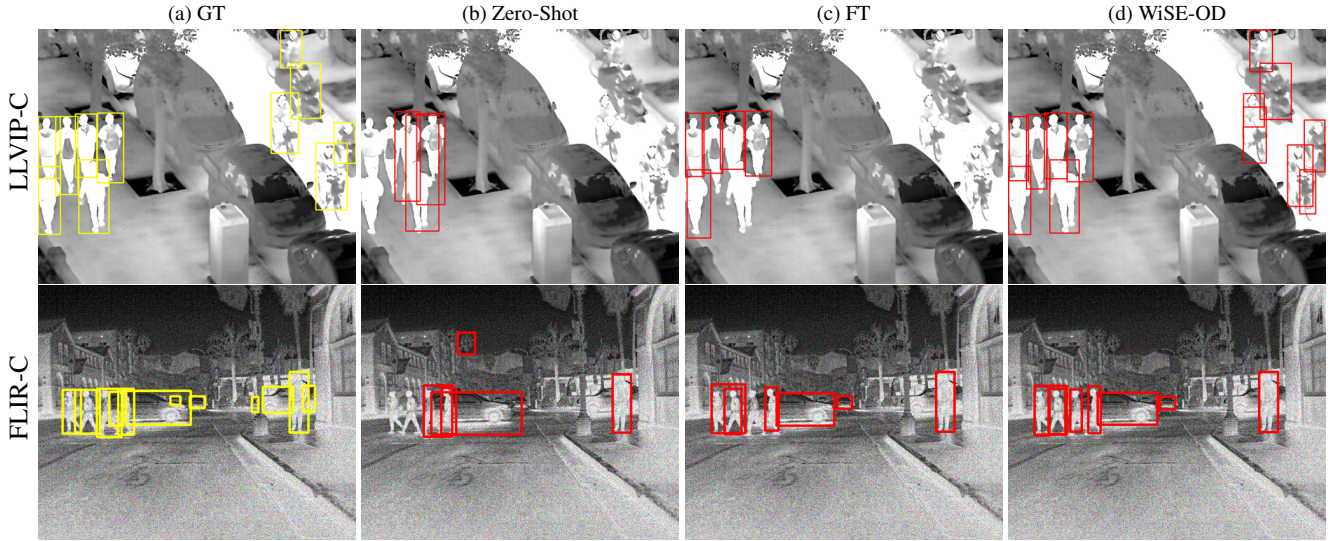


Figure 1. **Robustness in Infrared Object Detection on LLVIP-C and FLIR-C datasets.** In the first row, LLVIP-C has a brightness corruption severity level of 5; in the second row, FLIR-C shot noise corruption has a severity level of 2. In a) ground truth in yellow, b) zero-shot COCO detection, c) fine-tuning (FT), and d) WiSE-OD for Faster R-CNN detector.

Abstract

Object detection (OD) in infrared (IR) imagery is critical for low-light and nighttime applications. However, the scarcity of large-scale IR datasets forces models to rely on weights pre-trained on RGB images. While fine-tuning on IR improves accuracy, it often compromises robustness under distribution shifts due to the inherent modality gap between RGB and IR. To address this, we introduce LLVIP-C and FLIR-C, two cross-modality out-of-distribution (OOD) benchmarks built by applying corruption to standard IR datasets. Additionally, to fully leverage the complementary knowledge from RGB and infrared trained models, we propose WiSE-OD, a weight-space ensembling method with two variants: WiSE-OD_{ZS}, which combines RGB zero-shot and IR fine-tuned weights, and WiSE-OD_{LP}, which blends zero-shot and linear probing. Evaluated across three RGB-pretrained detectors and two robust baselines, WiSE-

OD improves both cross-modality and corruption robustness without any additional training or inference cost.¹

1. Introduction

In recent years, deep learning (DL) has achieved significant success across various computer vision tasks, including object detection (OD) [25] using thermal infrared (IR) imaging [13, 14]. Unlike visible spectrum imaging (RGB), which relies on reflected light, thermal IR imaging captures the heat emitted by objects, allowing it to function independently of lighting conditions. This makes IR-based OD highly effective in challenging environments with limited or absent visible light, such as night-time surveillance and autonomous driving cars [19]. Despite these advantages, IR OD models must maintain consistent performance and

¹Our code is available at: <https://github.com/heitorrapela/wiseod.git>

reliable predictions despite variations in input, due to occlusions, viewpoint shifts, or image degradation. Ensuring such robustness is therefore essential for real-world applications in surveillance [2, 16], autonomous driving [15], and defense [10], where fluctuating environmental conditions can impact sensor inputs and compromise system reliability.

Without large-scale IR pre-training datasets, OD models for IR typically initialize from powerful models pre-trained on large-scale RGB datasets (e.g., COCO [7]), followed by fine-tuning on IR data. While this pipeline yields strong in-domain (ID) performance, where ID refers to test samples similar to the training data, it often compromises robustness against out-of-domain (OOD) samples [3]. OOD samples differ significantly from the training data, leading to performance degradation. This deterioration stems from the fact that the fine-tuning process tends to cause the model to prioritize task-specific information at the expense of broader knowledge acquired during pre-training. As a result, the model struggles to generalize to new or diverse scenarios [22]. This issue is further amplified by the already substantial modality shift between RGB and IR, making robust transfer learning even more difficult [12]. In classification, several techniques have been proposed to improve robustness under distribution shifts, including linear probing (LP), LP followed by fine-tuning (LP-FT) [6], and weight-space ensembling (WiSE-FT) [22]. While these methods effectively enhance robustness in classification, they either are not directly applicable to object detection or remain under-explored [22]. This is because of the complex detection architectures and robustness, which demand both accurate localization and classification. Moreover, cross-modality adaptation from RGB to infrared (IR) introduces additional challenges due to the modality shift and the scarcity of large-scale IR data [12–14].

To address these challenges, in this paper, we introduce two key components: a novel cross-modality RGB/IR corruption benchmark, and two efficient approaches to improve average performance in the IR OOD corruption setting without additional training or inference cost. Our benchmark, LLVIP-C and FLIR-C, applies common corruption transforms to the original LLVIP and FLIR datasets to evaluate cross-modality OOD performance. Using this benchmark, we assess three families of IR ODs fine-tuned from RGB pre-trained models against standard robust fine-tuning baselines. Our analysis shows that traditional methods underperform in corruption settings; therefore, we introduced WiSE-OD, a simple approach that preserves the original detection head to combine zero-shot and fine-tuned weights, yielding WiSE-OD_{ZS} and its linear probing variation WiSE-OD_{LP}. We empirically found that these weight-space ensembling methods exhibit significant robustness. Additional analysis across various levels of cor-

ruption demonstrates that these methods improve average IR model performance by preserving the ID accuracy from fine-tuning and OOD robustness from zero-shot weights, which explains their effectiveness.

Our main contributions can be summarized as follows:

- A new benchmark, LLVIP-C and FLIR-C, is introduced to advance the evaluation of robust cross-modality OD between RGB and IR. This benchmark is essential for measuring detector performance across diverse, real-world conditions. Within this framework, we comprehensively evaluate three widely used object detection models: Faster R-CNN, FCOS, and RetinaNet, each initialized with COCO pre-trained weights.
- WiSE-OD with two variations: WiSE-OD_{ZS} and WiSE-OD_{LP}, is proposed for OD, an efficient technique to combine zero-shot and finetuned weights, enhancing the robustness under distribution shift.
- Extensive experiments are conducted on the proposed benchmark and our WiSE-OD technique, demonstrating a significant gain in performance over three OD frameworks.

2. Related Works

Object detection. OD is one of the most challenging computer vision tasks [9], especially due to many different environmental conditions [15]. The objective of OD is to localize with a bounding box and provide labels for all objects in an image [23]. Commonly, detectors can be categorized into two different groups: one-stage and two-stage detectors. The most famous and traditional two-stage detector is the Faster R-CNN [17], which first generates regions of interest and then uses a second classifier to confirm object presence within those regions. On the contrary, one-stage detectors eliminate the proposal generation stage, which focuses on real-time inference speed. On the one-stage detectors group, RetinaNet [8] utilizes a focal loss to address the class imbalance. Also, models like FCOS [20] have emerged in this category, eliminating predefined anchor boxes to potentially enhance inference efficiency. Our work focuses on these three traditional and powerful detectors: Faster R-CNN, RetinaNet, and FCOS.

Robustness in Object Detection. Robustness in OD refers to the model’s ability to maintain performance despite variations in input conditions. Hendrycks & Dietterich [3] proposed diverse corruptions for classification datasets, resulting in ImageNet-C and CIFAR10-C. Michaelis et al. [15] extended this to OD, proposing Pascal-C, COCO-C, and Cityscapes-C with a study on corruption severity and detector performance. Beghdadi et al. [1] introduced additional local transformations for RGB OD on COCO, and Mao et al. [11] proposed COCO-O with six types of

natural distribution shifts. Despite growing efforts for RGB OD robustness, IR OD still lacks such benchmarks. In this direction, Josi et al. [5] applied classification corruptions to IR for person ReID. Given the widespread use of IR in surveillance and autonomous driving, a robustness benchmark for IR OD is essential.

Robust Fine-Tuning. The deep learning community has explored various fine-tuning (FT) strategies to improve robustness in classification tasks. A common approach is linear probing (LP), where the backbone is frozen and only the head is trained. Kumar et al. [6] extended this with LP-FT, which first trains a linear head before unfreezing the backbone for full fine-tuning. Wortsman et al. [22] proposed WiSE-FT, which ensembles the weights of a zero-shot pretrained model and its fine-tuned counterpart in weight space, showing strong performance under distribution shifts on ImageNet.

In this work, we adapt these robustness techniques, which were originally developed for classification, to the more challenging cross-modality object detection setting, offering simple yet effective strategies to mitigate corruption effects. In the next section, we introduce our proposed IR OD benchmark and baselines.

3. Background

In this section, we introduce preliminary definitions that are necessary to understand this work, and subsequently, we define our proposed benchmark.

Object Detection. Consider a set of training samples $\mathcal{D} = \{(x_i, B_i)\}$, where $x_i \in \mathbb{R}^{W \times H \times C}$ are images with spatial resolution $W \times H$ and C channels, and $B_i = \{b_0, b_1, \dots, b_N\}$ is a set of bounding boxes corresponding image x_i . Each bounding box can be represented as $b = (c_x, c_y, w, h, o)$ where c_x and c_y are the center coordinates of the bounding box with size $w \times h$ and o is the class label. During training we aim to learn a parameterized function $f_\theta : \mathbb{R}^{W \times H \times C} \rightarrow \mathcal{B}$, with \mathcal{B} being the family of sets B_i and θ the model’s parameters vector. The optimization of f_θ is guided by a combination of a regression \mathcal{L}_r and classification \mathcal{L}_c loss, i.e., l_2 loss and binary cross-entropy, respectively. The loss function for object detection can be represented as:

$$\mathcal{L}_d(\theta) = \frac{1}{|\mathcal{D}|} \sum_{(x, B) \in \mathcal{D}} \mathcal{L}_c(f_\theta(x), B) + \lambda \mathcal{L}_r(f_\theta(x), B). \quad (1)$$

Robustness to Corruption. Corruption robustness measures a classifier’s average performance under classifier-agnostic input distortions [3]. Let $f : \mathcal{X} \rightarrow \mathcal{Y}$ be a classifier trained on samples drawn from a distribution \mathcal{Q} ,

and let $C = \{c : \mathcal{X} \rightarrow \mathcal{X}\}$ be a set of corruption functions (e.g. noise, blur, contrast) and $\mathcal{E} = \{e : \mathcal{X} \rightarrow \mathcal{X}\}$ a set of additional perturbation functions. The classifier’s clean accuracy is $\mathbb{P}_{(x, y) \sim \mathcal{Q}}(f(x) = y)$. Its corruption robustness, i.e., its expected accuracy under all compositions of one corruption and one perturbation, can be represented as:

$$\mathbb{E}_{c \sim C} \mathbb{E}_{e \sim \mathcal{E}} \left[\mathbb{P}_{(x, y) \sim \mathcal{Q}}(f(e(c(x))) = y) \right].$$

Weight-space Ensembling. Given a mixing coefficient $\lambda \in [0, 1]$, weight-space ensembling can be defined as the following function:

$$f_{\text{wse}}(\theta_i, \theta_j; \lambda) = (1 - \lambda) \theta_i + \lambda \theta_j, \quad (2)$$

which computes the element-wise convex combination of two parameter vectors θ_i and θ_j . The resulting ensemble parameter $\theta_{\text{ens}} = f_{\text{wse}}(\theta_i, \theta_j; \lambda)$ is then used to initialize the model for prediction. A notable example of this technique is WiSE-FT [22]. Moreover, weight-space ensembling builds on principles of output-space ensemble averaging [4] and has demonstrated improved OOD robustness on classification benchmarks [21].

4. OD IR Robustness Benchmark

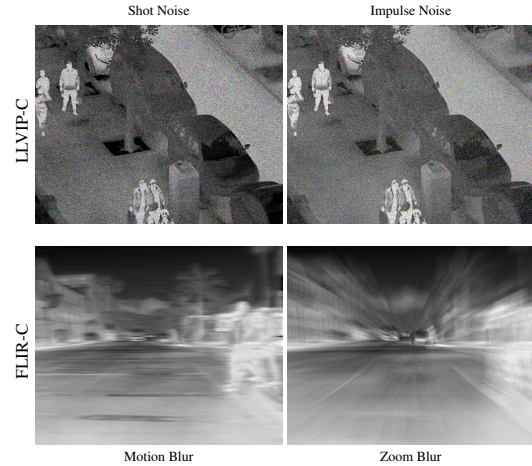


Figure 2. **LLVIP-C and FLIR-C examples.** First row, we have one example from the LLVIP-C test set with two different corruptions: Shot Noise, and Impulse Noise with a severity level of 5. In the second row, we have one example from the FLIR-C test set with Motion Blur and Zoom Blur with a severity level of 5.

4.1. Benchmark Datasets

For our proposed robust IR OD benchmark, we explore two classical datasets containing paired RGB and infrared images: LLVIP and FLIR.

LLVIP: The LLVIP dataset is a surveillance dataset composed of 12,025 paired IR and RGB images for training

and 3,463 paired IR and RGB images for testing. The resolution of images is 1280×1024 pixels, and annotations consist of bounding boxes around pedestrians.

FLIR ALIGNED: For the FLIR dataset, we used the sanitized and aligned paired sets provided [24], which contains 4,129 paired IR and RGB images for training, and 1,013 paired IR and RGB images for testing. The FLIR images are captured by a front-mounted car camera at a resolution of 640×512 pixels, and annotations contain bicycles, dogs, cars, and people.

LLVIP-C and FLIR-C: In this section, we present our two corrupted benchmarks: LLVIP-C and FLIR-C, derived from the LLVIP and FLIR datasets. In Figure 2, the first row shows an LLVIP-C test example corrupted with Shot Noise and Impulse Noise at severity level 5. The second row shows an FLIR-C test example corrupted with Motion Blur and Zoom Blur at severity level 5. As illustrated qualitatively, severity level 5 is too strong for the FLIR images, already compressed JPEGs, and both zero-shot and fine-tuned models perform worse on FLIR-C than on LLVIP-C at this level. Therefore, we recommend a maximum corruption severity of 2 for FLIR-C based on qualitative and quantitative results. For the following experiments, we use severity level 5 for LLVIP-C and severity level 2 for FLIR-C.

5. WiSE-OD

Our proposed method, WiSE-OD (f_{wod}) in Figure 3, extends the idea of WiSE-FT to object detection setting. Let θ_{RGB}^{COCO} and θ_{IR}^{FT} denote the parameters of the RGB pretrained COCO detector and the fully fine-tuned IR detection models, respectively. WiSE-OD constructs a new detector by interpolating these parameter vectors in weight space:

$$f_{wod}(\theta_{RGB}^{COCO}, \theta_{IR}^{FT}; \lambda) = (1 - \lambda) \theta_{RGB}^{COCO} + \lambda \theta_{IR}^{FT}. \quad (3)$$

The resulting interpolated model inherits both the broad generalization of large-scale COCO pretraining and the modality-specific accuracy of IR fine-tuning, yet requires no extra modules or change to the inference pipeline, only a one-time weight merge. We evaluate two variants: WiSE-OD_{ZS} uses θ_{IR}^{FT} (full fine-tuning), and WiSE-OD_{LP} uses θ_{IR}^{LP} (linear probing on the detection head with a frozen backbone). Both variants consistently improve robustness under domain shift and common corruptions, while maintaining the same inference cost as a single detector. This weight-space ensembling is model-agnostic and can be extended to fuse multiple checkpoints or modalities by hierarchical interpolation.

Metrics: Following the methodology for benchmarking robustness in OD [15], we select AP₅₀ as our detection performance metric for both LLVIP-C and FLIR-C evaluations.

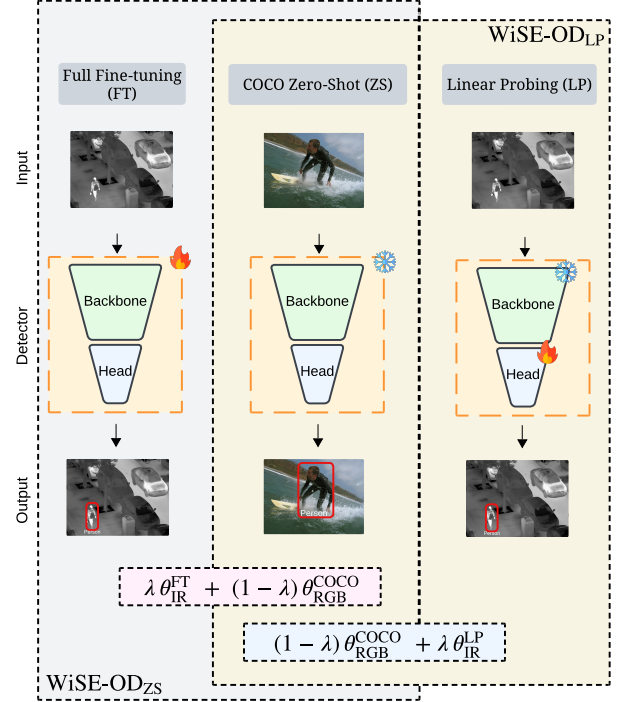


Figure 3. **Our proposed method: WiSE-OD and its variants.** In the large grey box, we have WiSE-OD_{ZS} with the equation inside the pink square, and WiSE-OD_{LP} in the yellow large box with the equation inside the blue square.

We also report the dataset-specific performance (P), defined as the AP₅₀ on the original target dataset (infrared), and the mean performance under corruption, mPC, defined as:

$$mPC = \frac{1}{N_c} \sum_{c=1}^{N_c} P_c, \quad (4)$$

where P_c is the AP₅₀ under corruption, and mPC is the average over all the corruptions. In our case, $N_c = 14$, we decided to remove the glass blur corruption because it lacks fast implementation for our benchmark.

Baseline models: In our study, we utilize three OD architectures: Faster R-CNN, FCOS, and RetinaNet, all initialized with COCO pre-trained weights. These models are trained on the COCO dataset, which contains 80 object categories, providing strong initial performance for most detection tasks and facilitating subsequent fine-tuning. We evaluate the following robust fine-tuning methods using our proposed benchmark:

1. **Zero-Shot (ZS)** – Unmodified detectors used directly for deployment without any fine-tuning.
2. **Linear probing (LP)** – Train the classification and regression heads on top of a frozen backbone by minimiz-

ing the detection loss.

3. **Full fine-tuning (FT)** – Update both the detection heads and the backbone parameters by minimizing the detection loss.
4. **LP-FT** – A two-stage process in which we first apply linear probing and then perform full fine-tuning initialized from the LP stage.
5. **Weight-ensembling** – Two variants, WiSE-OD_{ZS} and WiSE-OD_{LP} , which interpolate parameters between the zero-shot or linear-probing models and the fully fine-tuned models, respectively.

6. Experiments and Results

6.1. Training protocol

For this work, we split each training dataset into 80% for training and 20% for validation, reserving the original test set for final evaluation. All models were implemented in PyTorch, optimized with the Adam optimizer, and trained on an NVIDIA A100 GPU. We set a maximum training budget of 200 epochs for all detectors; in practice, fine-tuning typically converges within 10–20 epochs, depending on the model and dataset. We used a cosine annealing scheduler on the training loss and applied early stopping based on validation AP_{50} .

6.2. Benchmark Quantitative Results

In this section, we measured the mPC performance of all the proposed baselines for our benchmark on LLVIP-C with a severity level of 5 and the FLIR-C dataset with a severity level of 2. Results are shown in Table 2 for Faster R-CNN, FCOS, and RetinaNet under zero-shot, FT, LP, LP-FT, WiSE-OD_{ZS} , and WiSE-OD_{LP} . We see in Table 2, on average, WiSE-OD_{ZS} with λ fixed at 0.5, i.e., equal weighting of Zero-Shot and FT, outperforms all other baselines without the need to tune any hyperparameters. For instance, on LLVIP-C, WiSE-OD_{ZS} improved mPC by 18.68 over FT and by 4.12 over LP for Faster R-CNN. In most cases, our proposed variant WiSE-OD_{LP} outperformed WiSE-OD_{ZS} for Faster R-CNN and RetinaNet.

6.3. Detection performance per corruption

In this section, we evaluated the benchmark per corruption. For Table 1, we show the in-domain performance (evaluation on infrared of the LLVIP dataset), which we named “Original”, which is the original LLVIP infrared test set. Then, we have the corruptions for the LLVIP-C and the mPC metric for the Faster R-CNN detector; the same methodology was used for FLIR and FLIR-C. The original performance is measured in terms of AP_{50} for Faster R-CNN; additional results for FCOS, RetinaNet, and all the detectors are provided in the supplementary material. As described in the Table 1, the in-domain performance for LP

(91.82) and LP-FT (92.18) is lower than the FT (93.63), but the mPC is much higher than the zero-shot and FT. For instance, we have 70.96 for LP and 70.02 mPC for LP-FT (LP-FT was lower in OOD compared to LP), but its in-domain performance for LP-FT was a bit higher than LP. The FT was able to beat LP and LP-FT in the in-domain performance, but the mPC for FT was 56.40, which is 14.56 lower than LP and 13.62 lower than LP-FT. The WiSE-OD_{ZS} and WiSE-OD_{LP} were able to outperform the others with in-domain of 96.06 and 96.24, respectively, and for the mPC, the WiSE-OD_{LP} had 75.83 and the WiSE-OD_{ZS} 75.08, which the WiSE-OD_{ZS} is an increase of 18.68 from the original FT and 4.12 mPC over LP. For FLIR-C, we also have good improvements compared to the others. It is important to mention that the WiSE-OD_{ZS} is a free-training technique, and for this table, λ is fixed at 0.5, same for WiSE-OD_{LP} , but this variation needs the LP model instead of the zero-shot.

6.4. Performance over different corruption levels

In this section, we measured the per AP_{50} performance for Faster R-CNN, FCOS, and RetinaNet over different corruption severity levels for the benchmark. Here, in Figure 4, we provided the Frost for LLVIP-C and Fog for FLIR-C for Faster R-CNN. When the corruption severity level increases, e.g., from 1 to 5 in LLVIP-C, we can see a large drop in the zero-shot and FT, while the WiSE-OD_{ZS} is more stable and can bring more robustness to the final model. Some corruptions have more impact than others for each dataset; for instance, in FLIR-C, the noise corruption affected the performance more due to the original low-quality images. On IR modality, the contrast perturbation seems to affect the detection performance more because the images are already bad in contrast when compared to natural RGB images. A similar trend of stability of WiSE-OD_{ZS} for other detectors and corruptions over zero-shot and FT is shown in the supp. materials.

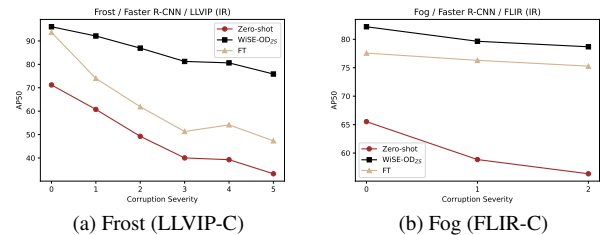


Figure 4. AP_{50} performance for Faster R-CNN over different corruption severity levels for Frost (a) and Fog (b). For each perturbation, we evaluated different levels of corruption for the Zero-Shot, WiSE-OD_{ZS} , and FT models. Here, we provide the Frost on LLVIP-C and Fog on FLIR-C. Additional study in supp. materials.

Table 1. **AP₅₀ performance over the perturbations on different datasets.** For LLVIP-C with severity level 5, and FLIR-C with severity level 2 for Faster R-CNN.

LLVIP-C						
	Zero-Shot	FT	LP	LP-FT	WiSE-OD _{ZS}	WiSE-OD _{LP}
Original	71.21 ± 0.02	93.68 ± 0.86	91.82 ± 0.15	92.18 ± 0.03	96.06 ± 0.22	96.24 ± 0.03
Gaussian Noise	59.24 ± 0.07	67.46 ± 7.45	75.12 ± 0.12	72.51 ± 0.28	86.68 ± 0.44	85.45 ± 0.76
Shot Noise	51.48 ± 0.14	64.83 ± 7.79	70.82 ± 0.27	69.89 ± 0.26	85.26 ± 0.50	85.25 ± 0.12
Impulse Noise	56.62 ± 0.07	71.32 ± 6.33	78.31 ± 1.13	75.20 ± 0.86	88.54 ± 0.33	88.40 ± 0.15
Defocus Blur	47.90 ± 0.08	80.48 ± 3.60	84.31 ± 0.24	83.12 ± 0.05	89.74 ± 0.98	90.40 ± 0.03
Motion Blur	26.39 ± 0.23	78.32 ± 3.18	77.15 ± 0.33	75.13 ± 0.05	86.81 ± 0.71	87.02 ± 0.32
Zoom Blur	02.47 ± 0.02	11.18 ± 1.56	24.65 ± 0.39	17.46 ± 0.02	22.83 ± 2.44	27.08 ± 0.01
Snow	33.65 ± 0.01	13.46 ± 4.45	69.92 ± 0.14	69.34 ± 0.13	65.97 ± 1.90	65.28 ± 2.70
Frost	33.25 ± 0.38	47.32 ± 3.45	68.00 ± 0.27	66.93 ± 0.42	75.87 ± 0.39	74.85 ± 0.29
Fog	59.60 ± 0.10	50.90 ± 10.07	87.05 ± 0.07	87.33 ± 0.39	84.51 ± 3.80	88.17 ± 0.06
Brightness	41.77 ± 0.03	35.36 ± 6.97	71.47 ± 0.34	76.45 ± 0.14	82.10 ± 1.20	82.61 ± 0.92
Contrast	47.48 ± 0.04	00.00 ± 0.00	51.53 ± 0.03	48.93 ± 0.02	10.57 ± 3.82	14.30 ± 1.82
Elastic transform	52.42 ± 0.18	92.41 ± 0.93	86.30 ± 0.25	88.98 ± 0.14	94.72 ± 0.07	94.85 ± 0.14
Pixelate	03.95 ± 0.01	87.69 ± 2.67	65.35 ± 0.09	65.71 ± 0.04	85.06 ± 3.32	84.33 ± 0.05
JPEG compression	57.22 ± 0.02	88.93 ± 1.69	83.58 ± 0.07	83.32 ± 0.24	92.59 ± 1.22	93.73 ± 0.03
mPC	40.96	56.40	70.96	70.02	75.08	75.83

FLIR-C						
	Zero-Shot	FT	LP	LP-FT	WiSE-OD _{ZS}	WiSE-OD _{LP}
Gaussian Noise	31.21 ± 0.29	28.07 ± 2.91	41.99 ± 0.39	39.83 ± 0.44	42.49 ± 4.48	39.33 ± 0.36
Shot Noise	25.26 ± 0.12	15.73 ± 2.05	33.24 ± 0.23	33.15 ± 0.43	30.45 ± 3.96	35.84 ± 0.46
Impulse Noise	17.69 ± 0.03	13.22 ± 2.27	26.15 ± 0.46	25.58 ± 0.46	22.51 ± 2.78	26.72 ± 0.18
Defocus Blur	25.32 ± 0.22	52.47 ± 0.99	44.57 ± 0.12	45.29 ± 0.20	54.08 ± 1.74	56.50 ± 1.22
Motion Blur	25.01 ± 0.25	51.71 ± 2.12	43.01 ± 0.41	42.79 ± 0.48	51.03 ± 2.16	57.24 ± 0.28
Zoom Blur	08.98 ± 0.05	17.97 ± 0.90	15.17 ± 0.02	14.17 ± 0.07	16.93 ± 1.00	19.34 ± 0.17
Snow	09.84 ± 0.14	07.86 ± 2.01	16.94 ± 0.31	19.57 ± 0.58	13.94 ± 2.66	16.31 ± 0.23
Frost	21.96 ± 0.50	33.87 ± 4.69	36.15 ± 0.29	37.82 ± 0.43	37.97 ± 3.63	38.80 ± 2.87
Fog	56.36 ± 0.28	73.61 ± 0.06	71.90 ± 0.37	71.26 ± 0.15	78.68 ± 1.24	78.10 ± 1.09
Brightness	64.41 ± 0.26	75.18 ± 0.99	74.92 ± 0.20	74.24 ± 0.10	79.72 ± 0.35	78.42 ± 0.17
Contrast	54.59 ± 0.04	75.47 ± 1.29	71.11 ± 0.13	70.60 ± 0.30	78.36 ± 1.06	79.72 ± 0.15
Elastic transform	41.88 ± 0.24	69.68 ± 1.15	64.49 ± 0.18	64.29 ± 0.06	73.39 ± 0.40	73.83 ± 0.54
Pixelate	38.67 ± 0.11	54.91 ± 6.21	55.61 ± 0.09	55.53 ± 0.13	61.12 ± 3.13	56.54 ± 0.01
JPEG compression	50.24 ± 0.14	57.55 ± 3.04	64.36 ± 0.30	62.82 ± 0.17	66.65 ± 0.89	65.70 ± 0.27
mPC	33.67	44.80	47.11	46.92	50.52	51.59

Table 2. **Detection performance for the OD IR Robustness Benchmark.** mPC metric for LLVIP-C with severity 5 and FLIR-C with severity level 2.

LLVIP-C						
Detector	Zero-Shot	FT	LP	LP-FT	WiSE-OD _{ZS}	WiSE-OD _{LP}
Faster R-CNN	40.96	56.40	70.96	70.02	75.08	75.83
FCOS	36.11	61.17	63.91	60.26	76.50	75.95
RetinaNet	37.50	61.13	60.37	61.11	73.69	74.39

FLIR-C						
Detector	Zero-Shot	FT	LP	LP-FT	WiSE-OD _{ZS}	WiSE-OD _{LP}
Faster R-CNN	33.67	44.80	47.11	46.92	50.52	51.59
FCOS	28.85	41.07	38.92	38.14	47.13	46.76
RetinaNet	28.27	42.71	36.71	36.45	45.35	47.53

6.5. Activation map analysis

In this section, we perform the qualitative analysis of the activation maps of the Faster R-CNN detector over the corruptions for the zero-shot model, WiSE-OD_{ZS}, and FT model over the corruptions on the LLVIP-C dataset. In Figure 5,

we can see the Grad-CAM [18] for impulse noise in the first row, then the zoom blur in the second row, with the ground-truth bounding box in red (additional activation maps figures for all the corruptions are provided in supp. materials). We see that the FT model and zero-shot do not detect the person well for such images under the corruptions, while for WiSE-OD_{ZS}, the detector was able to activate the features for a person even with the corruption, which means that it is more robust for such cases. However, in general, the WiSE-OD_{ZS} was able to activate more the person features in different corruptions than the FT; there are some corruption cases that it cannot detect as well as other ones; for such cases in which the user wants to perform better in a specific corruption for a real-world application, we recommend tuning the λ which can give more importance for the zero-shot weight or the FT depending on the corruption. Finally, we observed that WiSE-OD preserves more complete object regions in activation maps across both LLVIP-C and FLIR-C, particularly in corrupted images with low

contrast or fog. This suggests that ensembling retains complementary semantic cues from both zero-shot priors and fine-tuned details, leading to more stable predictions under corruptions.

Table 3. **Ablation of λ over LLVIP-C and FLIR-C dataset for Faster R-CNN.** Where $\lambda = 0.0$ represents the zero-shot model, $\lambda = 0.5$ represents default WiSE-OD_{ZS} and $\lambda = 1.0$ represents the fine-tuning model. For LLVIP-C, the severity level is 5.

LLVIP-C					
	$\theta(\lambda = 0.0)$	$\theta(\lambda = 0.2)$	$\theta(\lambda = 0.5)$	$\theta(\lambda = 0.8)$	$\theta(\lambda = 1.0)$
Original	71.21 \pm 0.02	93.88 \pm 0.28	96.06 \pm 0.22	95.41 \pm 0.60	93.68 \pm 0.86
Gaussian Noise	59.24 \pm 0.07	86.52 \pm 0.40	86.68 \pm 0.44	78.47 \pm 3.43	67.46 \pm 7.45
Shot Noise	51.48 \pm 0.14	83.86 \pm 0.70	85.26 \pm 0.50	76.42 \pm 3.74	64.83 \pm 7.79
Impulse Noise	56.62 \pm 0.07	86.93 \pm 0.65	88.54 \pm 0.33	80.94 \pm 2.70	71.32 \pm 6.33
Defocus Blur	47.90 \pm 0.08	88.41 \pm 0.31	89.74 \pm 0.98	85.85 \pm 2.55	80.48 \pm 3.60
Motion Blur	26.39 \pm 0.23	81.10 \pm 0.44	86.81 \pm 0.71	83.24 \pm 1.70	78.32 \pm 3.18
Zoom Blur	02.47 \pm 0.02	27.97 \pm 0.62	22.83 \pm 2.44	14.46 \pm 1.82	11.18 \pm 1.56
Snow	33.65 \pm 0.01	67.67 \pm 0.77	65.97 \pm 1.90	38.50 \pm 2.61	13.46 \pm 4.45
Frost	33.25 \pm 0.38	72.31 \pm 0.23	75.87 \pm 0.39	65.10 \pm 0.57	47.32 \pm 3.45
Fog	59.60 \pm 0.10	89.79 \pm 0.43	84.51 \pm 3.80	64.47 \pm 9.62	50.90 \pm 10.0
Brightness	41.77 \pm 0.03	82.38 \pm 0.17	82.10 \pm 1.20	62.81 \pm 3.16	35.36 \pm 6.97
Contrast	47.48 \pm 0.04	50.59 \pm 4.48	10.57 \pm 3.82	00.77 \pm 0.31	00.00 \pm 0.00
Elastic transform	52.42 \pm 0.18	89.92 \pm 0.51	94.72 \pm 0.07	94.32 \pm 0.34	92.41 \pm 0.93
Pixelate	03.95 \pm 0.01	66.27 \pm 3.14	85.06 \pm 3.32	88.97 \pm 2.35	87.69 \pm 2.67
JPEG compression	57.22 \pm 0.02	87.87 \pm 0.89	92.59 \pm 1.22	91.86 \pm 1.38	88.93 \pm 1.69
mPC	40.96	75.82	75.08	66.15	56.40

FLIR-C					
	$\theta(\lambda = 0.0)$	$\theta(\lambda = 0.2)$	$\theta(\lambda = 0.5)$	$\theta(\lambda = 0.8)$	$\theta(\lambda = 1.0)$
Original	65.52 \pm 0.07	77.49 \pm 0.10	82.20 \pm 0.07	80.18 \pm 0.11	77.57 \pm 0.24
Gaussian Noise	31.21 \pm 0.29	42.62 \pm 2.92	42.49 \pm 4.48	34.85 \pm 3.85	28.07 \pm 2.91
Shot Noise	25.26 \pm 0.12	33.91 \pm 2.98	30.45 \pm 3.96	21.88 \pm 2.93	15.73 \pm 2.05
Impulse Noise	17.69 \pm 0.03	24.85 \pm 2.26	22.51 \pm 2.78	16.96 \pm 2.17	13.22 \pm 2.27
Defocus Blur	25.32 \pm 0.22	44.57 \pm 2.40	54.08 \pm 1.74	55.00 \pm 0.98	52.47 \pm 0.99
Motion Blur	25.01 \pm 0.25	40.63 \pm 2.17	51.03 \pm 2.16	53.85 \pm 2.19	51.71 \pm 2.12
Zoom Blur	08.98 \pm 0.05	13.72 \pm 0.97	16.93 \pm 1.00	18.32 \pm 1.09	17.97 \pm 0.90
Snow	09.84 \pm 0.14	14.55 \pm 2.07	13.94 \pm 2.66	10.36 \pm 2.48	07.86 \pm 2.01
Frost	21.96 \pm 0.50	33.37 \pm 2.39	37.97 \pm 3.63	36.47 \pm 4.00	33.87 \pm 4.69
Fog	56.36 \pm 0.28	72.17 \pm 0.86	78.68 \pm 1.24	78.11 \pm 1.49	73.61 \pm 0.06
Brightness	64.41 \pm 0.26	75.68 \pm 0.19	79.72 \pm 0.35	77.79 \pm 1.24	75.18 \pm 0.99
Contrast	54.59 \pm 0.04	71.38 \pm 0.95	78.36 \pm 1.06	78.02 \pm 1.09	75.47 \pm 1.29
Elastic transform	41.88 \pm 0.24	63.89 \pm 0.37	73.39 \pm 0.40	72.51 \pm 0.58	69.68 \pm 1.15
Pixelate	38.67 \pm 0.11	55.23 \pm 2.37	61.12 \pm 3.13	58.87 \pm 4.58	54.91 \pm 6.21
JPEG compression	50.24 \pm 0.14	63.21 \pm 0.56	66.65 \pm 0.89	63.27 \pm 2.36	57.55 \pm 3.04
mPC	33.67	46.41	50.52	48.30	44.80

6.6. WiSE-OD_{ZS}: Ablation study on λ

In this section, we extensively conducted studies about the λ value to combine the zero-shot RGB COCO pre-training weights of Faster R-CNN, FCOS, and RetinaNet with the FT IR under the respective datasets LLVIP-C and FLIR-C. Evaluating the performance of such weight ensembling WiSE-OD_{ZS} under the different corruptions settings. Here, in the main manuscript, we show the results for Faster R-CNN in Table 3 for some values of λ , and we provide the detailed ablation and additional results in the supplementary material. It is important to mention that in the rest of the main manuscript, λ was fixed to 0.5, while here, we wanted to further investigate the potential of the WiSE-OD_{ZS} over the different corruptions. In Table 3, the best results for in-domain performance was with $\lambda = 0.5$, while the best out-of-domain was $\lambda = 0.2$, which shows that for Faster R-CNN the zero-shot model can bring robustness for the model, but some corruptions such as pixelate are better

when the λ is higher.

We observe that $\lambda = 0.5$ consistently provides a favorable trade-off, even for FLIR-C, where $\lambda = 0.5$ was the best ID. For LLVIP-C, WiSE-OD achieved the best mean performance under corruption ($\lambda = 0.2$, mPC 75.82), outperforming both the pure fine-tuned model ($\lambda = 1.0$, mPC 56.40) and the zero-shot model ($\lambda = 0.0$, mPC 40.96). Notably, $\lambda = 0.5$ performs best under heavy corruptions such as Gaussian noise, Fog, and Brightness shifts, scenarios where both FT and ZS individually struggle. For example, under Fog and Brightness, $\lambda = 0.5$ yields 84.51 and 82.10, respectively, while $\lambda = 1.0$ achieves only 50.90 and 35.36. This highlights the benefit of WiSE-OD in preserving complementary robustness features from both models. Interestingly, $\lambda = 0.8$ performs well in several cases but shows more variability, suggesting that moderate ensembling (rather than heavily biasing toward FT) is more robust under distribution shifts. These results justify the use of $\lambda = 0.5$ as a robust default and motivate future work on adaptive λ selection strategies.

6.7. Limitations

Main Limitations. While WiSE-OD demonstrates robust performance across corruption types and detectors, it has certain limitations. First, the method assumes access to both a zero-shot model and a fine-tuned or linearly probed counterpart, which may not always be feasible in constrained deployment scenarios. Second, the fixed mixing coefficient λ , although effective at 0.5 in general, may not be optimal for all corruption types or datasets. As shown in our ablation study, tuning λ for specific perturbations can yield better results, suggesting that an adaptive λ selection mechanism could further enhance performance. Additionally, the method’s effectiveness is tied to the quality of the pretrained models; for instance, if the zero-shot or fine-tuned models underperform due to poor initialization or training instability, the ensemble will inherit those weaknesses. Lastly, our study focuses on robustness to synthetic corruptions and may not fully capture all real-world distribution shifts, such as hardware-specific noise or extreme weather conditions.

Failure cases. Despite its strong average performance across corruption types, WiSE-OD is not without failure cases. We observe that its robustness can degrade under extreme conditions such as severe snow, heavy blur, or very low brightness, particularly in the FLIR-C dataset. In these settings, both the zero-shot and fine-tuned models tend to misfire, either missing objects entirely or generating fragmented predictions, causing the ensemble to inherit and even amplify these errors. Furthermore, in scenes with high thermal clutter or indistinct object boundaries, the fusion of weights may lead to uncertain activations and unstable bounding boxes. These failure modes highlight the importance of complementary improvements such as corruption-

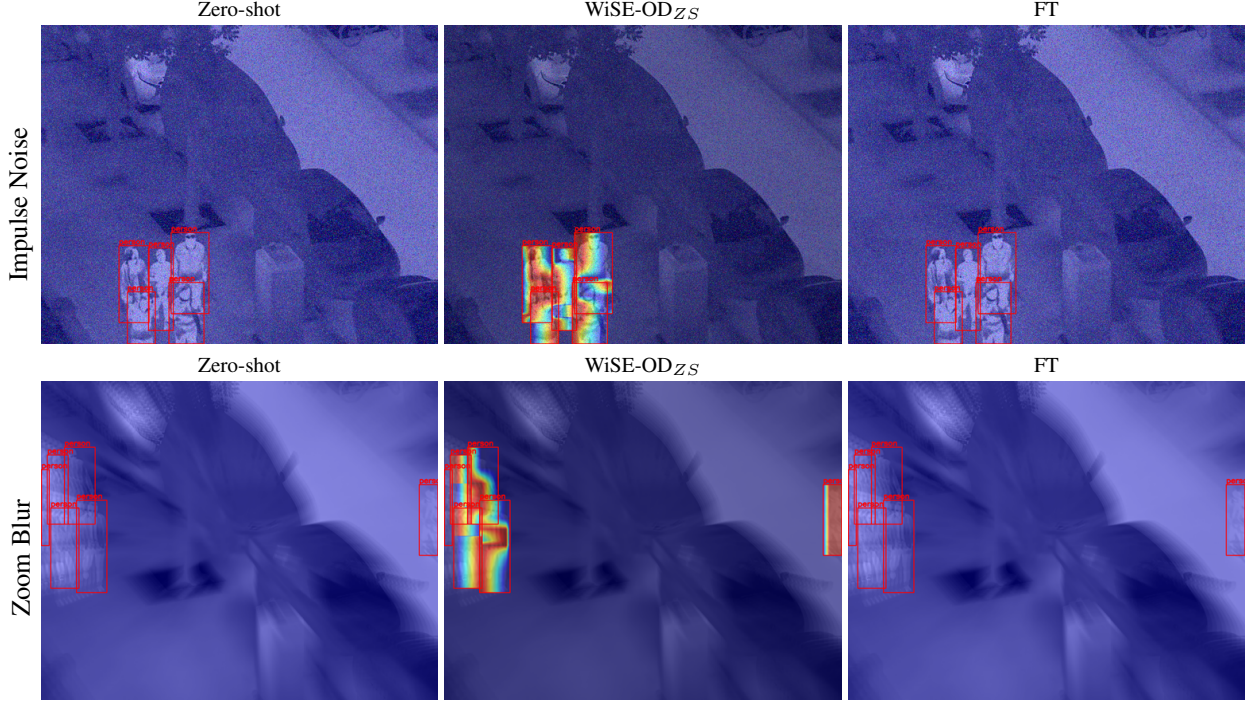


Figure 5. **Activation map analysis for zero-shot COCO pre-train Faster R-CNN detector, the WiSE-OD_{ZS} and FT detector on IR for LLVIP-C dataset.** In red are the GTs, and for the WiSE-OD_{ZS}, the models can activate the features that represent a person for such corruptions (The first row is impulse noise, and the second row is the zoom blur with a severity of 5).

aware ensembling or dynamic λ adjustment.

6.8. Final Discussion and Future Work

Our findings suggest that simple weight-space ensembling strategies can significantly improve robustness in cross-modality detection. However, one promising direction is to make these ensembles adaptive. Rather than using a fixed λ , one could explore data-driven mechanisms, e.g., predicting λ per image or corruption type using a lightweight auxiliary network. Another natural extension is to ensemble more than two model variants (e.g., LP, FT, multiple seeds) to form model soups for detection, which have shown improvements in classification. Additionally, while our current benchmark focuses on synthetic corruptions adapted from ImageNet-C, future benchmarks could incorporate real-world IR degradations, such as thermal blooming, lens fogging, or sensor-specific quantization artifacts. Moreover, exploring the integration of WiSE-OD with domain generalization methods or meta-learning approaches could yield more adaptive solutions in unseen IR environments. Finally, applying our method to other sensor modalities like depth, multispectral, or event-based data could reveal whether WiSE-OD generalizes beyond IR, positioning it as a lightweight alternative to domain adaptation and robustness training pipelines. Additionally, future works could explore adaptive or corruption-aware weight blending and

extend the benchmark to broader domain shifts like day-night transitions or different IR sensors.

7. Conclusion

In this work, we presented a new benchmark for robustness IR OD based on the work of Hendrycks and Dietterich [3], with the target of traditional IR datasets such as LLVIP and FLIR. Our new benchmark is a challenging setting for IR robustness with the introduction of LLVIP-C and FLIR-C. Furthermore, we did an extensive study of different robust fine-tuning strategies over our proposed benchmark. Additionally, we present the WiSE-OD method and its variations WiSE-OD_{ZS} and WiSE-OD_{LP}, where both were able to surpass the traditional robustness strategies while also increasing in-domain performance over different detectors, such as Faster R-CNN, FCOS, and RetinaNet. Our extensive study shows that a simple but WiSE-OD strategy can mitigate performance drop without any additional training cost.

Acknowledgments

This work was supported in part by Distech Controls Inc., the Natural Sciences and Engineering Research Council of Canada, the Digital Research Alliance of Canada, and MITACS.

WiSE-OD: Benchmarking Robustness in Infrared Object Detection

Supplementary Material

In this supplementary material, we provide additional information to reproduce our work². This supplementary material is divided into the following sections: Dataset Visualization (Section 8), Detection performance per corruption (Section 9), Activation map analysis (Section 10), WiSE-OD_{ZS}: Ablation study on λ (Section 11) and Performance over different corruption levels (Section 12).

8. Dataset Visualization

In this section, we provide additional visualization of each corruption for both datasets: LLVIP-C in Figure 6 and FLIR-C in Figure 7. Here, we wanted to highlight how strong the severity level of 5 is for FLIR-C, which can destroy the whole image, for instance, for the Frost corruption.

9. Detection performance per corruption

In this section, we expanded our evaluation of the benchmark per corruption. In the main manuscript, we provided the results per corruption for Faster R-CNN with a severity level of 5 for LLVIP-C. Here, we provide the additional results for the FCOS (Table 4) and RetinaNet (Table 5) for LLVIP-C, FCOS (Table 6) and RetinaNet (Table 7) for FLIR-C with severity level of 2.

Table 4. AP₅₀ performance over the perturbations for LLVIP-C with severity level 5 for FCOS.

LLVIP-C						
	Zero-Shot	FT	LP	LP-FT	WiSE-OD _{ZS}	WiSE-OD _{LP}
Gaussian Noise	55.03 ± 0.07	62.32 ± 5.96	73.63 ± 0.09	64.46 ± 0.42	83.68 ± 0.67	81.78 ± 0.08
Shot Noise	43.83 ± 0.36	58.75 ± 5.48	66.05 ± 1.98	59.34 ± 0.08	80.55 ± 0.81	80.00 ± 0.59
Impulse Noise	51.60 ± 0.17	65.26 ± 5.31	68.98 ± 0.04	65.06 ± 0.21	85.86 ± 0.53	85.21 ± 0.95
Defocus Blur	33.67 ± 0.00	80.30 ± 1.90	78.14 ± 0.00	76.47 ± 0.00	87.74 ± 0.68	88.77 ± 0.00
Motion Blur	15.09 ± 0.34	78.87 ± 1.09	70.67 ± 0.21	67.88 ± 0.25	84.32 ± 0.76	84.06 ± 0.01
Zoom Blur	01.28 ± 0.00	20.13 ± 2.95	18.75 ± 0.87	14.01 ± 0.00	31.47 ± 2.96	30.27 ± 0.00
Snow	37.37 ± 0.25	33.17 ± 2.74	45.72 ± 0.31	42.42 ± 0.25	69.72 ± 1.83	70.94 ± 0.38
Frost	35.33 ± 0.07	60.18 ± 1.17	53.68 ± 1.07	48.67 ± 0.37	76.33 ± 1.12	74.94 ± 1.47
Fog	55.52 ± 0.13	69.47 ± 4.86	85.08 ± 0.02	81.24 ± 0.19	89.49 ± 0.56	90.45 ± 0.05
Brightness	36.46 ± 0.00	55.69 ± 2.98	65.16 ± 0.00	65.88 ± 0.00	82.52 ± 0.90	82.84 ± 0.00
Contrast	42.04 ± 0.00	00.64 ± 0.74	56.61 ± 0.21	49.36 ± 0.00	23.45 ± 4.15	20.26 ± 0.00
Elastic transform	43.02 ± 0.09	92.96 ± 0.57	83.77 ± 0.15	83.65 ± 0.22	93.97 ± 0.38	93.67 ± 0.03
Pixelate	02.14 ± 0.00	88.12 ± 0.65	55.20 ± 0.00	54.17 ± 0.00	89.43 ± 0.90	88.50 ± 0.00
JPEG compression	53.22 ± 0.00	90.53 ± 1.18	73.40 ± 0.00	71.14 ± 0.00	92.59 ± 0.40	91.71 ± 0.00
mPC	36.11	61.17	63.91	60.26	76.50	75.95

10. Activation map analysis

In this section, we provide more plots with the Grad-CAM activations. Here, we divided into three figures due to space constraints: Figure 8, Figure 9, and Figure 10. In many cases, the WiSE-OD_{ZS} had a person detected on average, which is shown by the red highlighted part of the images.

²Our code is available at: <https://github.com/heitorrapela/wiseod.git>

Table 5. AP₅₀ performance over the perturbations for LLVIP-C with severity level 5 for RetinaNet.

LLVIP-C						
	Zero-Shot	FT	LP	LP-FT	WiSE-OD _{ZS}	WiSE-OD _{LP}
Gaussian Noise	52.52 ± 0.21	70.55 ± 8.23	66.70 ± 0.19	66.32 ± 0.25	82.63 ± 3.59	88.10 ± 0.07
Shot Noise	44.70 ± 0.22	64.02 ± 10.87	57.85 ± 0.13	59.03 ± 0.17	78.94 ± 4.68	78.14 ± 1.53
Impulse Noise	48.17 ± 0.19	73.01 ± 6.68	66.97 ± 1.82	67.78 ± 0.08	84.19 ± 3.05	86.53 ± 1.95
Defocus Blur	43.13 ± 0.00	75.38 ± 8.71	71.92 ± 0.00	73.08 ± 0.20	84.31 ± 3.89	88.45 ± 0.00
Motion Blur	18.79 ± 0.07	71.69 ± 9.38	62.14 ± 0.15	63.62 ± 0.17	79.92 ± 4.78	78.59 ± 3.16
Zoom Blur	01.61 ± 0.00	12.73 ± 3.63	09.21 ± 0.00	09.93 ± 0.55	21.02 ± 5.04	16.92 ± 0.00
Snow	35.54 ± 0.34	36.48 ± 11.52	56.68 ± 0.14	55.19 ± 0.18	71.09 ± 5.52	72.05 ± 4.35
Frost	36.52 ± 0.06	57.94 ± 6.50	53.83 ± 0.26	53.47 ± 0.32	75.35 ± 3.81	78.60 ± 1.74
Fog	58.48 ± 0.21	65.31 ± 6.58	83.18 ± 0.27	82.28 ± 0.06	85.07 ± 2.92	84.11 ± 0.12
Brightness	39.03 ± 0.00	54.83 ± 8.34	69.76 ± 1.69	70.79 ± 0.00	82.41 ± 1.89	80.70 ± 0.00
Contrast	49.09 ± 0.00	00.99 ± 0.00	52.12 ± 0.00	54.61 ± 2.76	13.90 ± 1.79	13.64 ± 1.58
Elastic transform	37.37 ± 0.04	93.05 ± 1.27	76.89 ± 0.07	77.56 ± 1.20	94.52 ± 0.07	94.18 ± 0.09
Pixelate	03.86 ± 0.00	88.82 ± 1.97	48.35 ± 0.00	49.68 ± 0.00	85.68 ± 2.38	89.83 ± 0.00
JPEG compression	56.24 ± 0.00	91.09 ± 1.73	69.68 ± 0.00	72.32 ± 2.93	92.67 ± 1.14	91.71 ± 0.00
mPC	37.50	61.13	60.37	61.11	73.69	74.39

Table 6. AP₅₀ performance over the perturbations for FLIR-C with severity level 2 for FCOS.

FLIR-C						
	Zero-Shot	FT	LP	LP-FT	WiSE-OD _{ZS}	WiSE-OD _{LP}
Gaussian Noise	23.65 ± 0.16	24.76 ± 2.44	32.89 ± 0.41	31.78 ± 1.07	38.53 ± 1.47	38.35 ± 1.20
Shot Noise	17.63 ± 0.26	15.39 ± 1.80	27.41 ± 0.17	25.10 ± 0.12	27.85 ± 1.06	30.10 ± 0.43
Impulse Noise	14.12 ± 0.23	11.34 ± 0.88	20.93 ± 0.53	18.22 ± 0.05	21.07 ± 1.25	23.10 ± 0.19
Defocus Blur	19.23 ± 0.00	44.40 ± 1.40	33.08 ± 0.00	32.27 ± 0.32	48.14 ± 1.00	48.75 ± 0.85
Motion Blur	20.77 ± 0.21	43.17 ± 1.44	33.95 ± 0.62	33.58 ± 0.31	45.65 ± 1.29	48.20 ± 0.50
Zoom Blur	6.73 ± 0.00	15.32 ± 0.14	11.81 ± 0.00	11.17 ± 0.00	15.44 ± 0.52	16.38 ± 0.54
Snow	8.29 ± 0.32	07.63 ± 1.31	12.32 ± 0.18	13.04 ± 0.22	12.50 ± 1.08	11.42 ± 0.14
Frost	19.23 ± 0.26	30.80 ± 0.69	28.14 ± 0.27	27.60 ± 0.35	35.68 ± 0.55	36.37 ± 0.69
Fog	51.56 ± 0.07	70.56 ± 0.41	63.60 ± 0.53	62.12 ± 0.14	74.39 ± 0.84	72.79 ± 0.26
Brightness	58.43 ± 0.00	69.69 ± 1.05	64.79 ± 0.00	64.78 ± 0.00	75.59 ± 0.94	73.02 ± 0.17
Contrast	50.28 ± 0.00	70.41 ± 0.96	62.97 ± 0.10	61.36 ± 0.00	73.99 ± 0.69	73.02 ± 0.33
Elastic transform	36.76 ± 0.48	64.18 ± 0.74	54.62 ± 0.82	52.40 ± 0.75	68.95 ± 0.52	66.47 ± 0.32
Pixelate	32.65 ± 0.00	51.74 ± 0.86	45.58 ± 0.00	47.96 ± 0.00	59.03 ± 0.09	57.42 ± 0.00
JPEG compression	44.71 ± 0.00	55.63 ± 0.96	52.90 ± 0.00	52.61 ± 0.00	63.03 ± 0.74	59.33 ± 0.00
mPC	28.85	41.07	38.92	38.14	47.13	46.76

Table 7. AP₅₀ performance over the perturbations for FLIR-C with severity level 2 for RetinaNet.

FLIR-C						
	Zero-Shot	FT	LP	LP-FT	WiSE-OD _{ZS}	WiSE-OD _{LP}
Gaussian Noise	25.61 ± 0.20	26.47 ± 3.14	33.34 ± 0.38	31.44 ± 0.52	34.31 ± 2.83	33.09 ± 0.26
Shot Noise	19.36 ± 0.06	16.95 ± 2.60	25.49 ± 0.26	24.16 ± 0.26	24.15 ± 2.42	29.00 ± 0.85
Impulse Noise	14.82 ± 0.17	15.90 ± 1.98	18.58 ± 0.28	19.12 ± 0.28	21.77 ± 1.50	24.58 ± 0.37
Defocus Blur	19.30 ± 0.00	46.15 ± 1.86	31.28 ± 0.00	30.62 ± 0.00	44.74 ± 1.61	48.43 ± 0.63
Motion Blur	20.05 ± 0.16	45.96 ± 3.97	29.39 ± 0.11	30.28 ± 0.16	42.91 ± 2.90	50.99 ± 0.23
Zoom Blur	07.05 ± 0.00	15.99 ± 1.06	10.48 ± 0.00	10.55 ± 0.00	15.40 ± 0.32	16.03 ± 0.00
Snow	07.91 ± 0.16	08.34 ± 1.84	09.29 ± 0.08	09.54 ± 0.34	11.09 ± 1.44	12.80 ± 1.38
Frost	17.63 ± 0.32	33.90 ± 3.17	24.81 ± 0.34	24.31 ± 0.44	33.02 ± 2.41	36.32 ± 0.31
Fog	48.95 ± 0.13	70.48 ± 0.40	60.61 ± 0.11	60.32 ± 0.11	72.46 ± 0.50	74.75 ± 1.09
Brightness	56.74 ± 0.00	70.06 ± 0.30	61.90 ± 0.00	63.21 ± 0.00	74.80 ± 0.56	74.52 ± 1.18
Contrast	47.50 ± 0.00	70.75 ± 0.38	59.36 ± 0.00	59.94 ± 0.00	71.89 ± 0.43	74.44 ± 0.48
Elastic transform	34.27 ± 0.34	65.63 ± 0.54	50.84 ± 0.50	49.74 ± 0.42	68.19 ± 0.54	68.58 ± 1.09
Pixelate	32.52 ± 0.00	55.52 ± 1.21	45.84 ± 0.00	45.96 ± 0.00	57.66 ± 0.30	59.29 ± 0.00
JPEG compression	44.10 ± 0.00	55.89 ± 0.86	52.80 ± 0.00	51.23 ± 0.00	62.57 ± 1.02	62.71 ± 0.00
mPC	28.27	42.71	36.71	36.45	45.35	47.53

11. WiSE-OD_{ZS}: Ablation study on λ

In this section, we expanded our ablation study. In the Table 8, we have the full study for Faster R-CNN with LLVIP-C and in Table 9 for FLIR-C, as well as the FCOS in Table 10 and RetinaNet in Table 11. As mentioned in the main manuscript, the $\lambda = 0.5$ has a good performance under corruption without having to tune the λ over a validation set,

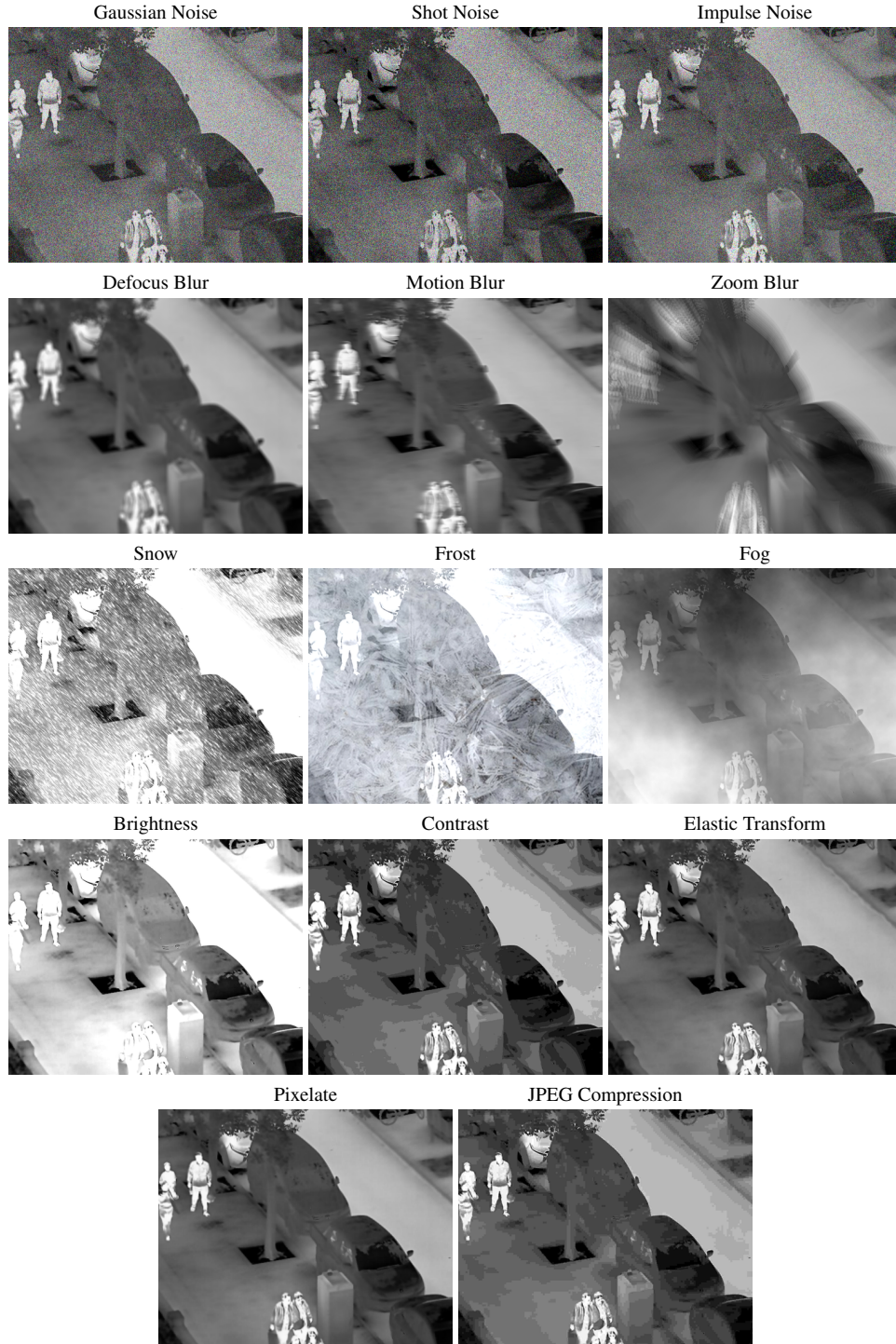


Figure 6. All the 14 corruptions types from [3], adapted to our LLVIP-C benchmark with severity of 5.

so it is a good choice for most of the cases; to be better in a specific corruption, we could tune the λ .

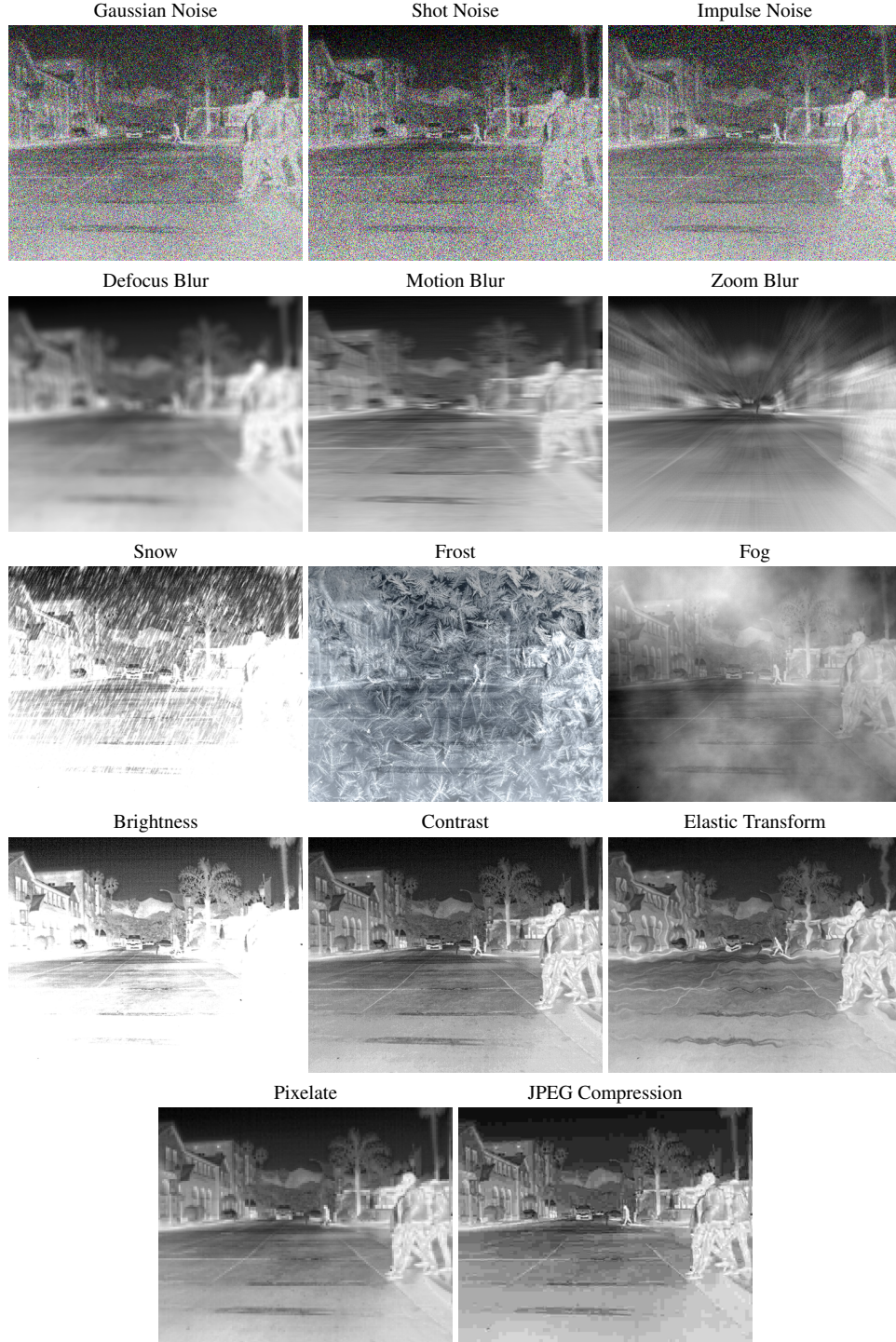


Figure 7. All the 14 corruptions types from [3], adapted to our FLIR-C benchmark with severity of 5.

12. Performance over different corruption levels

In this section, we measured the per AP_{50} performance for Faster R-CNN, FCOS, and RetinaNet over different corrup-

tion severity levels for the benchmark. Here, we focus on Zero-Shot, FT and $WiSE-OD_{ZS}$ for most of the corruptions on LLVIP-C illustrated in Figure 11 and Figure 12, and for FLIR-C in Figure 13 and Figure 14.

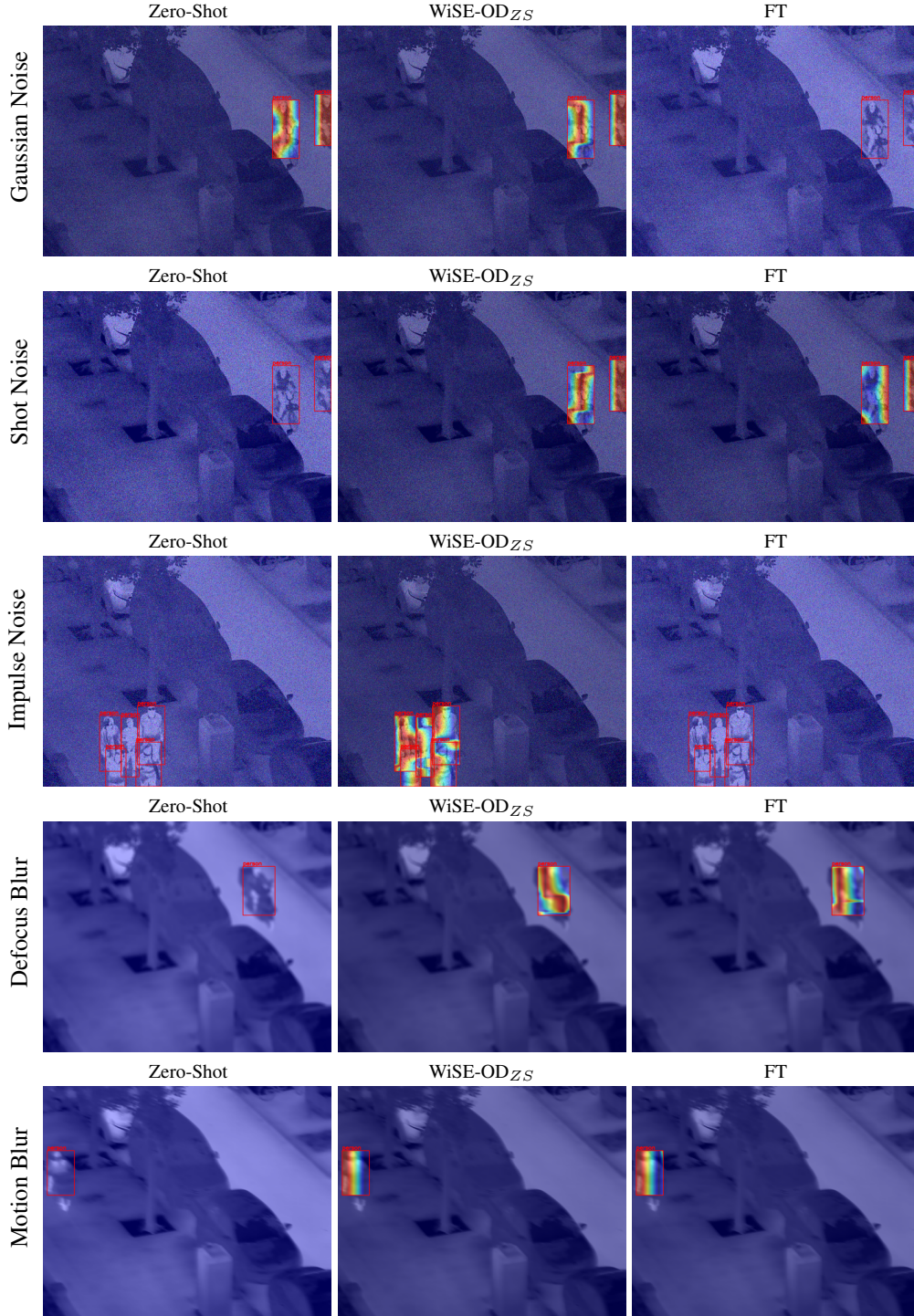


Figure 8. **Activation map analysis for zero-shot COCO pre-train Faster R-CNN detector, the WiSE-OD_{ZS} and FT detector on IR for LLVIP-C dataset.** In red are the GTs, and for the WiSE-OD_{ZS}, the models are able to activate the features that represent a person for such corruptions (Part 1 with 5 of the 14 corruptions).

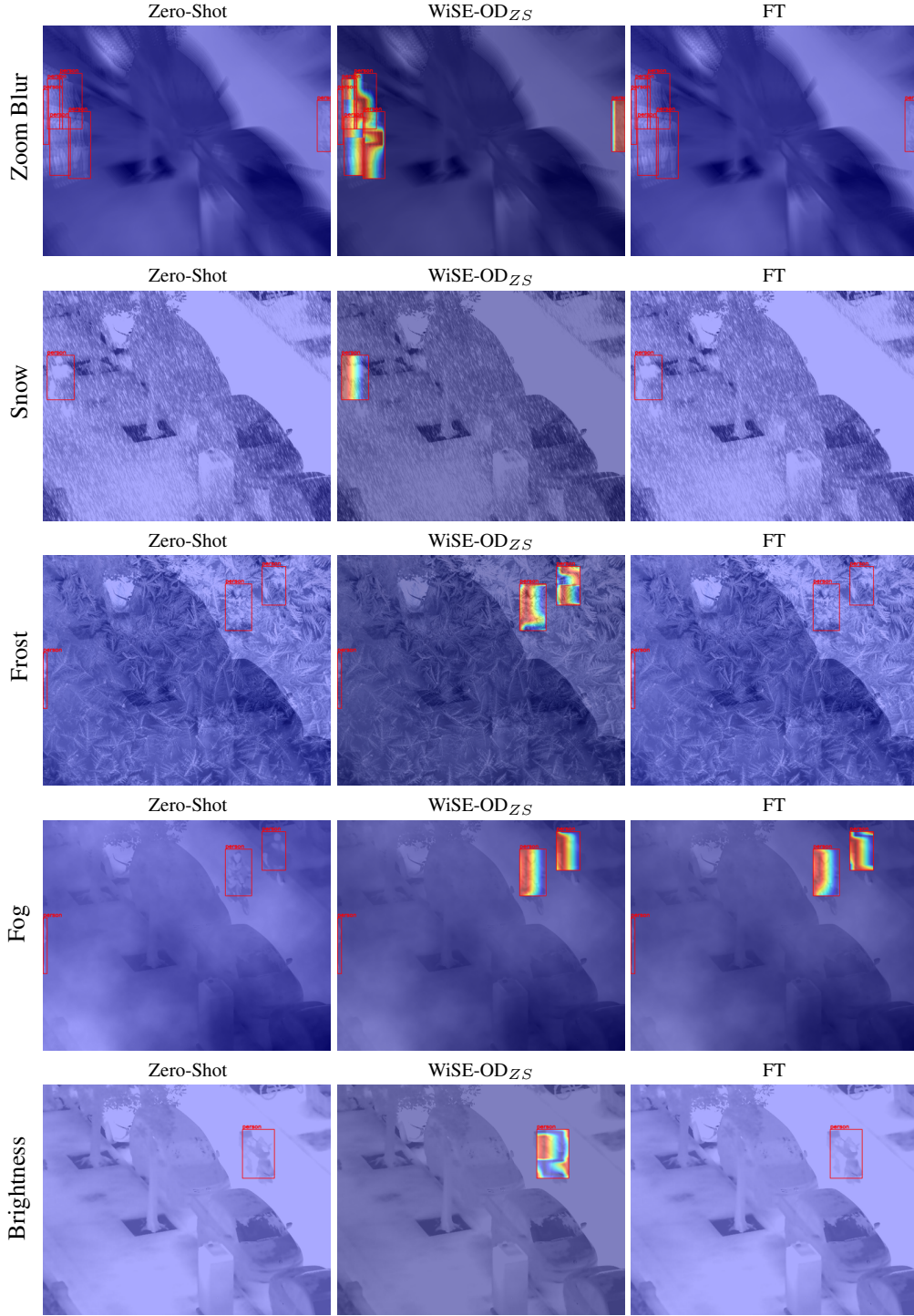


Figure 9. **Activation map analysis for zero-shot COCO pre-train Faster R-CNN detector, the WiSE-OD_{ZS} and FT detector on IR for LLVIP-C dataset.** In red are the GTs, and for the WiSE-OD_{ZS}, the models are able to activate the features that represent a person for such corruptions (Part 2 with 5 of the 14 corruptions).

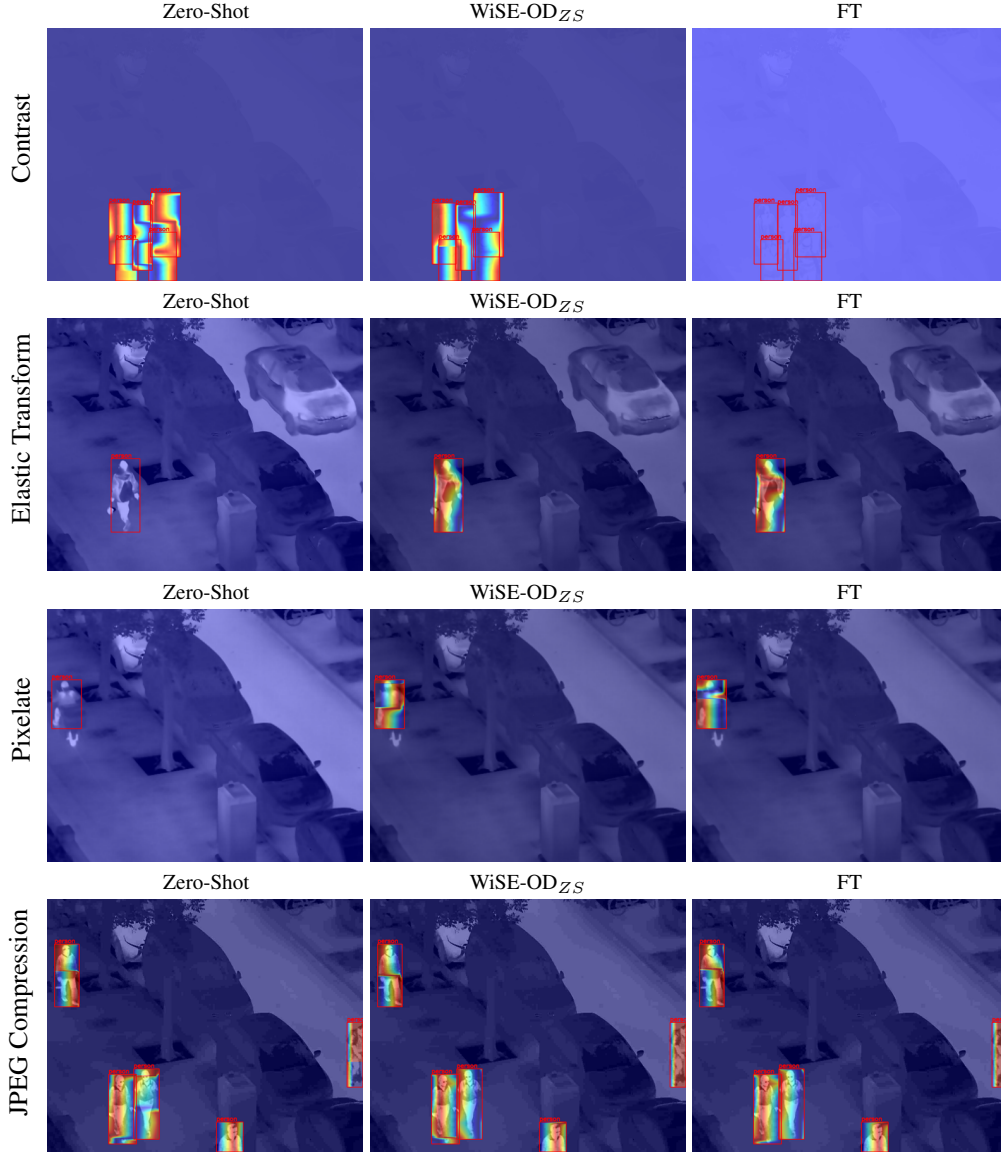


Figure 10. **Activation map analysis for zero-shot COCO pre-train Faster R-CNN detector, the WiSE-OD_{ZS} and FT detector on IR for LLVIP-C dataset.** In red are the GTs, and for the WiSE-OD_{ZS}, the models are able to activate the features that represent a person for such corruptions (Part 3 with 4 of the 14 corruptions).

Table 8. Ablation of λ over LLVIP-C dataset for Faster R-CNN. Where $\lambda = 0.0$ represents the zero-shot model, $\lambda = 0.5$ represents default WiSE-OD_{ZS} and $\lambda = 1.0$ represents the fine-tuning model. For LLVIP-C, the severity level is 5.

Test Set IR (Dataset: LLVIP-C)											
	$\theta(\lambda = 0.0)$	$\theta(\lambda = 0.1)$	$\theta(\lambda = 0.2)$	$\theta(\lambda = 0.3)$	$\theta(\lambda = 0.4)$	$\theta(\lambda = 0.5)$	$\theta(\lambda = 0.6)$	$\theta(\lambda = 0.7)$	$\theta(\lambda = 0.8)$	$\theta(\lambda = 0.9)$	$\theta(\lambda = 1.0)$
Original	71.21 ± 0.02	90.88 ± 0.12	93.88 ± 0.28	95.16 ± 0.10	95.73 ± 0.15	96.06 ± 0.22	96.03 ± 0.29	95.88 ± 0.33	95.41 ± 0.60	94.72 ± 0.53	93.68 ± 0.86
Gaussian Noise	59.24 ± 0.07	83.30 ± 0.26	86.52 ± 0.40	87.13 ± 0.50	87.34 ± 0.15	86.68 ± 0.44	85.04 ± 1.02	82.37 ± 1.94	78.47 ± 3.43	73.39 ± 5.44	67.46 ± 7.45
Shot Noise	51.48 ± 0.14	80.36 ± 0.15	83.86 ± 0.70	85.49 ± 0.60	86.00 ± 0.16	85.26 ± 0.50	83.47 ± 1.19	80.54 ± 2.08	76.42 ± 3.74	71.03 ± 5.67	64.83 ± 7.79
Impulse Noise	56.62 ± 0.07	82.52 ± 0.23	86.93 ± 0.65	88.47 ± 0.83	88.90 ± 0.32	88.54 ± 0.33	87.09 ± 0.89	84.64 ± 1.73	80.94 ± 2.70	76.78 ± 4.21	71.32 ± 6.33
Defocus Blur	47.90 ± 0.08	82.35 ± 0.29	88.41 ± 0.31	89.78 ± 0.61	90.22 ± 0.78	89.74 ± 0.98	88.89 ± 1.54	87.42 ± 2.19	85.85 ± 2.55	83.41 ± 3.10	80.48 ± 3.60
Motion Blur	26.39 ± 0.23	71.73 ± 0.89	81.10 ± 0.44	85.01 ± 0.23	86.54 ± 0.49	86.81 ± 0.71	86.30 ± 1.22	84.99 ± 1.56	83.24 ± 1.70	80.90 ± 2.21	78.32 ± 3.18
Zoom Blur	02.47 ± 0.02	20.59 ± 0.62	27.97 ± 0.62	28.10 ± 1.23	26.04 ± 2.00	22.83 ± 2.44	19.69 ± 2.18	17.03 ± 2.09	14.46 ± 1.82	12.63 ± 1.72	11.18 ± 1.56
Snow	33.65 ± 0.01	59.62 ± 0.70	67.67 ± 0.77	70.10 ± 0.36	69.55 ± 1.04	65.97 ± 1.90	59.54 ± 2.56	50.03 ± 3.09	38.50 ± 2.61	25.35 ± 3.58	13.46 ± 4.45
Frost	33.25 ± 0.38	63.68 ± 0.18	72.31 ± 0.23	75.45 ± 0.31	76.36 ± 0.33	75.87 ± 0.39	73.83 ± 0.27	70.41 ± 0.37	65.10 ± 0.57	57.51 ± 1.79	47.32 ± 3.45
Fog	59.60 ± 0.10	85.74 ± 0.04	89.79 ± 0.43	90.17 ± 0.96	88.01 ± 1.99	84.51 ± 3.80	78.78 ± 6.13	72.14 ± 8.00	64.47 ± 9.62	57.25 ± 10.1	50.90 ± 10.0
Brightness	41.77 ± 0.03	75.37 ± 0.17	82.38 ± 0.17	84.12 ± 0.20	84.07 ± 0.58	82.10 ± 1.20	78.20 ± 1.97	71.94 ± 2.81	62.81 ± 3.16	49.92 ± 4.49	35.36 ± 6.97
Contrast	47.48 ± 0.04	58.36 ± 1.99	50.59 ± 4.48	34.73 ± 5.82	20.25 ± 4.48	10.57 ± 3.82	04.99 ± 2.13	02.25 ± 1.17	00.77 ± 0.31	00.33 ± 0.47	00.00 ± 0.00
Elastic transform	52.42 ± 0.18	84.78 ± 0.42	89.92 ± 0.51	92.67 ± 0.27	94.10 ± 0.05	94.72 ± 0.07	94.94 ± 0.11	94.92 ± 0.17	94.32 ± 0.34	93.73 ± 0.36	92.41 ± 0.93
Pixelate	03.95 ± 0.01	42.41 ± 1.64	66.27 ± 3.14	76.01 ± 3.53	81.29 ± 3.70	85.06 ± 3.32	87.01 ± 2.91	88.18 ± 2.82	88.97 ± 2.35	88.75 ± 2.39	87.69 ± 2.67
JPEG compression	57.22 ± 0.02	82.36 ± 0.73	87.87 ± 0.89	90.49 ± 1.05	91.95 ± 1.11	92.59 ± 1.22	92.62 ± 1.25	92.42 ± 1.20	91.86 ± 1.38	90.53 ± 1.47	88.93 ± 1.69
mPC	40.96	69.51	75.82	76.98	76.47	75.08	72.88	69.94	66.15	61.53	56.40

Table 9. Ablation of λ over FLIR-C dataset for Faster R-CNN. Where $\lambda = 0.0$ represents the zero-shot model, $\lambda = 0.5$ represents default WiSE-OD_{ZS} and $\lambda = 1.0$ represents the fine-tuning model. For FLIR-C, the severity level is 2.

Test Set IR (Dataset: FLIR-C)											
	$\theta(\lambda = 0.0)$	$\theta(\lambda = 0.1)$	$\theta(\lambda = 0.2)$	$\theta(\lambda = 0.3)$	$\theta(\lambda = 0.4)$	$\theta(\lambda = 0.5)$	$\theta(\lambda = 0.6)$	$\theta(\lambda = 0.7)$	$\theta(\lambda = 0.8)$	$\theta(\lambda = 0.9)$	$\theta(\lambda = 1.0)$
Original	65.52 ± 0.07	73.51 ± 0.14	77.49 ± 0.10	79.74 ± 0.10	80.87 ± 0.09	82.20 ± 0.07	81.31 ± 0.17	80.95 ± 0.26	80.18 ± 0.11	79.03 ± 0.09	77.57 ± 0.24
Gaussian Noise	31.21 ± 0.29	38.94 ± 1.77	42.62 ± 2.92	44.05 ± 3.60	44.11 ± 4.31	42.49 ± 4.48	40.60 ± 4.35	37.88 ± 4.13	34.85 ± 3.85	31.43 ± 3.37	28.07 ± 2.91
Shot Noise	25.26 ± 0.12	31.53 ± 1.55	33.91 ± 2.98	33.86 ± 4.03	32.81 ± 4.12	30.45 ± 3.96	27.89 ± 3.63	24.81 ± 3.25	21.88 ± 2.93	18.79 ± 2.52	15.73 ± 2.05
Impulse Noise	17.69 ± 0.03	22.94 ± 1.52	24.85 ± 2.26	25.00 ± 2.70	24.15 ± 2.64	22.51 ± 2.78	21.18 ± 2.89	18.95 ± 2.49	16.96 ± 2.17	15.15 ± 2.33	13.22 ± 2.27
Defocus Blur	25.32 ± 0.22	37.37 ± 1.81	44.57 ± 2.40	49.45 ± 2.37	52.30 ± 2.01	54.08 ± 1.74	54.99 ± 1.38	55.33 ± 1.10	55.00 ± 0.98	54.01 ± 0.64	52.47 ± 0.99
Motion Blur	25.01 ± 0.25	34.24 ± 1.35	40.63 ± 2.17	45.17 ± 2.38	48.75 ± 2.17	51.03 ± 2.16	53.19 ± 2.13	53.96 ± 2.00	53.85 ± 2.19	53.29 ± 2.18	51.71 ± 2.12
Zoom Blur	08.98 ± 0.05	11.77 ± 0.49	13.72 ± 0.97	15.20 ± 1.01	16.10 ± 1.01	16.93 ± 1.00	17.69 ± 1.10	18.02 ± 1.11	18.32 ± 1.09	18.24 ± 0.94	17.97 ± 0.90
Snow	09.84 ± 0.14	13.39 ± 1.37	14.55 ± 2.07	15.19 ± 2.60	14.85 ± 2.69	13.94 ± 2.66	12.73 ± 2.68	11.47 ± 2.59	10.36 ± 2.48	08.99 ± 2.25	07.86 ± 2.01
Frost	21.96 ± 0.50	29.17 ± 1.92	33.37 ± 2.39	35.98 ± 2.87	37.34 ± 3.17	37.97 ± 3.63	37.71 ± 3.59	37.22 ± 3.82	36.47 ± 4.00	35.17 ± 4.45	33.87 ± 4.69
Fog	56.36 ± 0.28	67.20 ± 1.18	72.17 ± 0.86	75.52 ± 0.67	77.56 ± 0.97	78.68 ± 1.24	78.85 ± 1.00	78.71 ± 1.23	78.11 ± 1.49	76.92 ± 1.12	73.61 ± 0.06
Brightness	64.41 ± 0.26	71.92 ± 0.51	75.68 ± 0.19	75.60 ± 0.13	79.09 ± 0.49	79.72 ± 0.35	79.53 ± 0.96	78.56 ± 1.28	77.79 ± 1.24	76.54 ± 1.33	75.18 ± 0.99
Contrast	54.59 ± 0.04	66.11 ± 0.79	71.38 ± 0.95	74.78 ± 1.19	77.03 ± 0.90	78.36 ± 1.06	78.62 ± 1.12	78.36 ± 0.99	78.02 ± 1.09	76.87 ± 1.15	75.47 ± 1.29
Elastic transform	41.88 ± 0.24	55.93 ± 0.47	63.89 ± 0.37	68.62 ± 0.39	71.71 ± 0.79	73.39 ± 0.40	73.66 ± 0.41	73.37 ± 0.25	72.51 ± 0.58	71.51 ± 0.42	69.68 ± 1.15
Pixelate	38.67 ± 0.11	49.47 ± 1.66	55.23 ± 2.37	58.37 ± 2.52	60.02 ± 2.70	61.12 ± 3.13	60.93 ± 3.43	60.12 ± 4.13	58.87 ± 4.58	57.14 ± 5.60	54.91 ± 6.21
JPEG compression	50.24 ± 0.14	59.12 ± 0.61	63.21 ± 0.56	65.59 ± 0.63	66.55 ± 0.80	66.65 ± 0.89	66.12 ± 1.48	64.94 ± 1.84	63.27 ± 2.36	60.63 ± 2.39	57.55 ± 3.04
mPC	33.67	42.07	46.41	48.74	50.16	50.52	50.26	49.40	48.30	46.76	44.80

Table 10. Ablation of λ over FLIR-C dataset for FCOS. Where $\lambda = 0.0$ represents the zero-shot model, $\lambda = 0.5$ represents default WiSE-OD_{ZS} and $\lambda = 1.0$ represents the fine-tuning model. For FLIR-C, the severity level is 2.

Test Set IR (Dataset: FLIR-C)											
	$\theta(\lambda = 0.0)$	$\theta(\lambda = 0.1)$	$\theta(\lambda = 0.2)$	$\theta(\lambda = 0.3)$	$\theta(\lambda = 0.4)$	$\theta(\lambda = 0.5)$	$\theta(\lambda = 0.6)$	$\theta(\lambda = 0.7)$	$\theta(\lambda = 0.8)$	$\theta(\lambda = 0.9)$	$\theta(\lambda = 1.0)$
Original	59.90 ± 0.00	69.17 ± 0.00	73.37 ± 0.70	75.92 ± 0.61	76.42 ± 0.00	77.82 ± 0.00	76.13 ± 0.70	75.64 ± 1.17	73.84 ± 0.00	73.18 ± 1.00	71.78 ± 1.27
Gaussian Noise	23.65 ± 0.16	35.87 ± 0.60	39.92 ± 0.34	40.94 ± 0.69	40.21 ± 1.22	38.53 ± 1.47	36.49 ± 1.58	33.92 ± 1.84	31.18 ± 1.93	27.93 ± 2.20	24.76 ± 2.44
Shot Noise	17.63 ± 0.26	28.36 ± 0.75	31.61 ± 0.30	31.49 ± 0.15	30.10 ± 0.62	27.85 ± 1.06	25.41 ± 1.18	22.97 ± 1.38	20.49 ± 1.46	17.95 ± 1.66	15.39 ± 1.80
Impulse Noise	14.12 ± 0.23	22.48 ± 0.30	24.23 ± 0.54	23.70 ± 0.82	22.94 ± 1.06	21.07 ± 1.25	19.60 ± 0.93	17.57 ± 0.84	15.50 ± 0.70	13.98 ± 0.97	11.34 ± 0.88
Defocus Blur	19.23 ± 0.00	32.58 ± 0.60	39.97 ± 0.61	44.29 ± 1.13	46.66 ± 1.10	48.14 ± 1.00	48.96 ± 1.24	48.92 ± 1.33	47.87 ± 1.58	46.38 ± 1.54	44.40 ± 1.40
Motion Blur	20.77 ± 0.21	31.73 ± 0.59	37.81 ± 0.69	41.68 ± 1.03	44.17 ± 1.43	45.65 ± 1.29	46.54 ± 0.90	46.60 ± 0.96	46.01 ± 1.07	44.90 ± 1.19	43.17 ± 1.44
Zoom Blur	06.73 ± 0.00	11.12 ± 0.35	13.23 ± 0.43	14.27 ± 0.52	14.94 ± 0.54	15.44 ± 0.52	15.70 ± 0.51	15.89 ± 0.18	16.06 ± 0.19	15.91 ± 0.15	15.32 ± 0.14
Snow	08.29 ± 0.32	11.98 ± 0.26	13.57 ± 0.41	13.62 ± 0.71	13.19 ± 1.05	12.50 ± 1.08	11.63 ± 1.20	10.85 ± 1.26	09.83 ± 1.24	08.73 ± 1.22	07.63 ± 1.31
Frost	19.23 ± 0.26	28.62 ± 0.65	32.77 ± 0.39	34.68 ± 0.25	35.33 ± 0.38	35.68 ± 0.55	35.44 ± 0.77	34.87 ± 0.89	33.96 ± 0.73	32.55 ± 0.68	30.80 ± 0.69
Fog	51.56 ± 0.07	63.39 ± 0.15	68.76 ± 0.18	72.17 ± 0.55	73.84 ± 0.71	74.39 ± 0.84	74.45 ± 0.85	73.36 ± 1.40	72.63 ± 1.28	71.42 ± 1.25	70.56 ± 0.41
Brightness	58.43 ± 0.00	67.75 ± 0.15	72.80 ± 0.42	75.20 ± 0.50	75.88 ± 0.88	75.59 ± 0.94	74.73 ± 0.90	73.78 ± 1.00	72.72 ± 1.04	71.21 ± 1.10	69.69 ± 1.05
Contrast	50.28 ± 0.00	62.55 ± 0.12	68.03 ± 0.30	71.68 ± 0.53	73.50 ± 0.67	73.99 ± 0.69	73.83 ± 1.02	73.28 ± 1.39	72.75 ± 1.12	71.68 ± 1.15	70.41 ± 0.96
Elastic transform	36.76 ± 0.48	53.13 ± 0.82	61.25 ± 0.88	65.65 ± 0.70	67.93 ± 0.34	68.95 ± 0.52	68.84 ± 0.48	68.30 ± 0.81	67.21 ± 1.01	65.96 ± 1.01	64.18 ± 0.74
Pixelate	32.65 ± 0.00	45.53 ± 0.92	52.09 ± 0.78	55.86 ± 0.74	57.68 ± 0.95	59.03 ± 0.09	57.56 ± 0.54	57.57 ± 0.67	56.31 ± 0.63	54.36 ± 0.82	51.74 ± 0.86
JPEG compression	44.71 ± 0.00	55.25 ± 0.38	59.69 ± 0.05	62.18 ± 0.29	63.13 ± 0.58	63.03 ± 0.74	62.49 ± 0.45	61.14 ± 0.36	59.44 ± 0.34	57.37 ± 0.64	55.63 ± 0.96
mPC	28.85	39.31	43.98	46.24	47.10	47.13	46.54	45.64	44.42	42.88	41.07

Table 11. Ablation of λ over FLIR-C dataset for RetinaNet. Where $\lambda = 0.0$ represents the zero-shot model, $\lambda = 0.5$ represents default WiSE-OD_{ZS} and $\lambda = 1.0$ represents the fine-tuning model. For FLIR-C, the severity level is 2.

Test Set IR (Dataset: FLIR-C)											
	$\theta(\lambda = 0.0)$	$\theta(\lambda = 0.1)$	$\theta(\lambda = 0.2)$	$\theta(\lambda = 0.3)$	$\theta(\lambda = 0.4)$	$\theta(\lambda = 0.5)$	$\theta(\lambda = 0.6)$	$\theta(\lambda = 0.7)$	$\theta(\lambda = 0.8)$	$\theta(\lambda = 0.9)$	$\theta(\lambda = 1.0)$
Original	58.46 \pm 0.00	67.08 \pm 0.22	71.71 \pm 0.32	74.93 \pm 0.15	76.38 \pm 0.62	77.34 \pm 0.05	77.00 \pm 0.19	76.88 \pm 0.01	76.08 \pm 0.15	74.35 \pm 0.30	73.38 \pm 0.89
Gaussian Noise	25.61 \pm 0.20	32.69 \pm 0.58	35.32 \pm 0.84	35.81 \pm 1.74	35.33 \pm 2.47	34.31 \pm 2.83	33.28 \pm 2.92	31.93 \pm 3.02	30.34 \pm 3.13	28.58 \pm 3.11	26.47 \pm 3.14
Shot Noise	19.36 \pm 0.06	25.03 \pm 0.61	26.67 \pm 0.46	26.40 \pm 1.27	25.48 \pm 2.02	24.15 \pm 2.42	22.78 \pm 2.53	21.43 \pm 2.41	19.98 \pm 2.53	18.43 \pm 2.63	16.95 \pm 2.60
Impulse Noise	14.82 \pm 0.17	20.28 \pm 0.66	22.12 \pm 0.18	22.72 \pm 0.54	21.78 \pm 1.37	21.77 \pm 1.50	20.62 \pm 1.79	19.08 \pm 1.54	17.98 \pm 1.93	16.96 \pm 2.15	15.90 \pm 1.98
Defocus Blur	19.30 \pm 0.00	29.18 \pm 0.55	35.62 \pm 0.32	39.61 \pm 0.79	42.52 \pm 1.27	44.74 \pm 1.61	46.50 \pm 1.67	47.22 \pm 1.77	47.46 \pm 1.81	47.04 \pm 1.84	46.15 \pm 1.86
Motion Blur	20.05 \pm 0.16	26.99 \pm 0.15	32.06 \pm 0.46	36.34 \pm 1.21	39.83 \pm 2.32	42.91 \pm 2.90	45.13 \pm 3.39	46.75 \pm 3.63	47.25 \pm 3.87	46.89 \pm 3.94	45.96 \pm 3.97
Zoom Blur	07.05 \pm 0.00	10.04 \pm 0.26	11.99 \pm 0.40	13.25 \pm 0.26	14.43 \pm 0.28	15.40 \pm 0.32	16.07 \pm 0.52	16.43 \pm 0.65	16.52 \pm 0.81	16.37 \pm 0.93	15.99 \pm 1.06
Snow	07.91 \pm 0.16	09.65 \pm 0.25	10.62 \pm 0.40	11.12 \pm 0.85	11.29 \pm 1.21	11.09 \pm 1.44	10.83 \pm 1.73	10.40 \pm 1.91	09.79 \pm 1.88	09.06 \pm 1.91	08.34 \pm 1.84
Frost	17.63 \pm 0.32	23.01 \pm 0.57	26.44 \pm 0.96	29.27 \pm 1.55	31.40 \pm 1.95	33.02 \pm 2.41	34.19 \pm 2.59	34.95 \pm 2.84	34.91 \pm 3.13	34.53 \pm 3.04	33.90 \pm 3.17
Fog	48.95 \pm 0.13	58.32 \pm 0.38	64.25 \pm 0.24	68.23 \pm 0.25	70.96 \pm 0.45	72.46 \pm 0.50	73.24 \pm 0.26	73.41 \pm 0.45	72.88 \pm 0.24	71.92 \pm 0.28	70.48 \pm 0.40
Brightness	56.74 \pm 0.00	65.14 \pm 0.27	69.99 \pm 0.39	72.90 \pm 0.28	74.43 \pm 0.64	74.80 \pm 0.56	74.84 \pm 0.55	74.02 \pm 0.40	73.09 \pm 0.11	71.80 \pm 0.16	70.06 \pm 0.30
Contrast	47.50 \pm 0.00	56.81 \pm 0.50	62.87 \pm 0.31	67.26 \pm 0.07	70.04 \pm 0.23	71.89 \pm 0.43	72.81 \pm 0.27	73.09 \pm 0.20	72.80 \pm 0.10	71.94 \pm 0.12	70.75 \pm 0.38
Elastic transform	34.27 \pm 0.34	48.18 \pm 0.94	57.07 \pm 0.64	62.39 \pm 0.47	65.90 \pm 0.29	68.19 \pm 0.54	69.25 \pm 0.68	69.51 \pm 0.44	68.86 \pm 0.53	67.56 \pm 0.53	65.63 \pm 0.54
Pixelate	32.52 \pm 0.00	41.93 \pm 0.67	48.02 \pm 0.74	52.27 \pm 0.66	55.46 \pm 0.47	57.66 \pm 0.30	58.83 \pm 0.15	59.10 \pm 0.40	58.58 \pm 0.58	57.48 \pm 0.82	55.52 \pm 1.21
JPEG compression	44.10 \pm 0.00	52.89 \pm 0.51	57.47 \pm 0.47	60.21 \pm 0.60	61.79 \pm 0.86	62.57 \pm 1.02	62.33 \pm 0.77	61.31 \pm 0.63	59.89 \pm 0.65	58.10 \pm 0.54	55.89 \pm 0.86
mPC	28.27	35.72	40.03	42.69	44.33	45.35	45.76	45.61	45.02	44.04	42.71

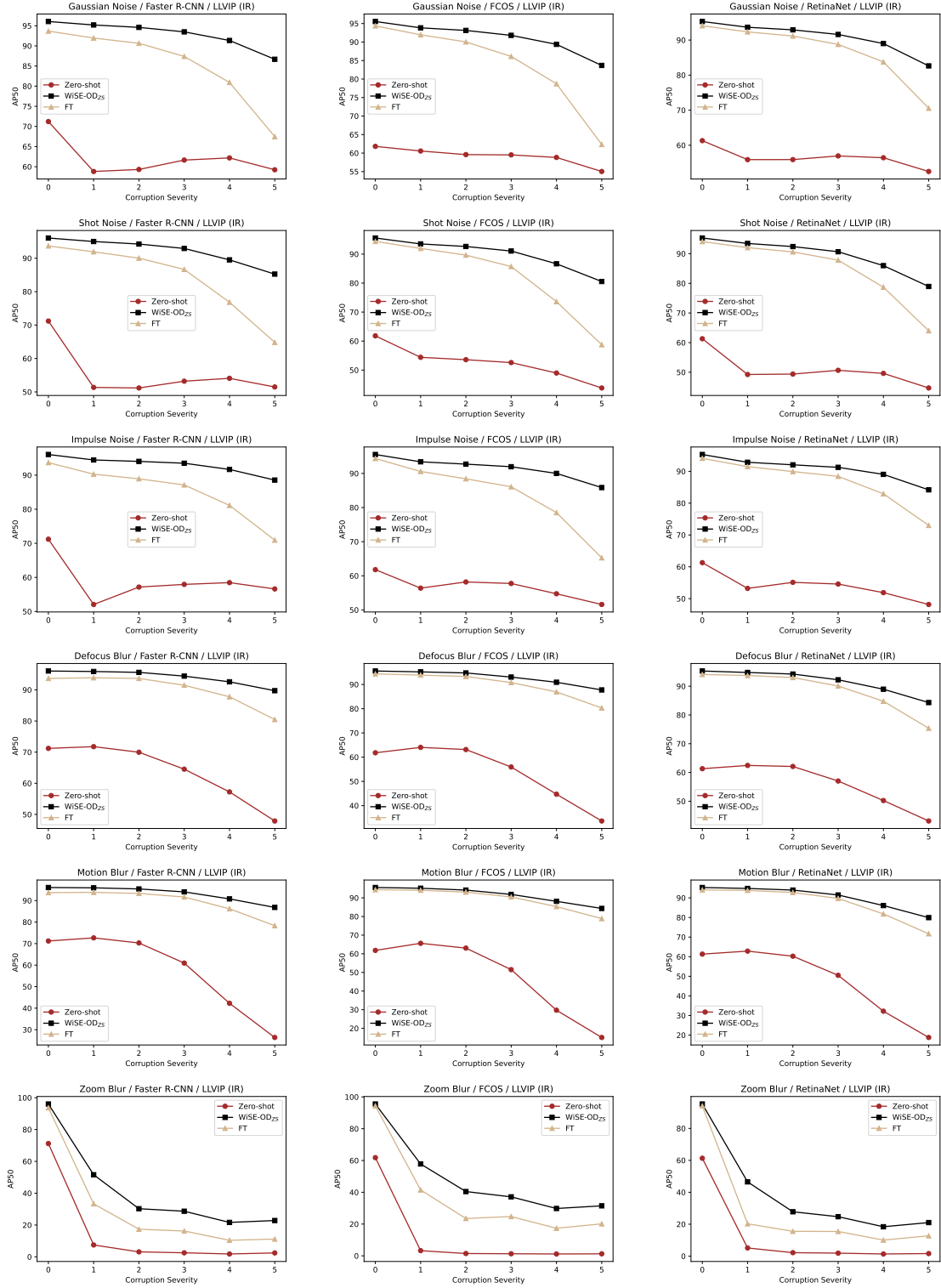


Figure 11. AP_{50} performance for all detectors over different corruption severity levels for Gaussian Noise, Shot Noise, Impulse Noise, Defocus Blur, Motion Blur and Zoom Blur. For each perturbation, we evaluated different levels of corruption for the Zero-Shot, WiSE-OD₂₅, and FT models for LLVIP-C.

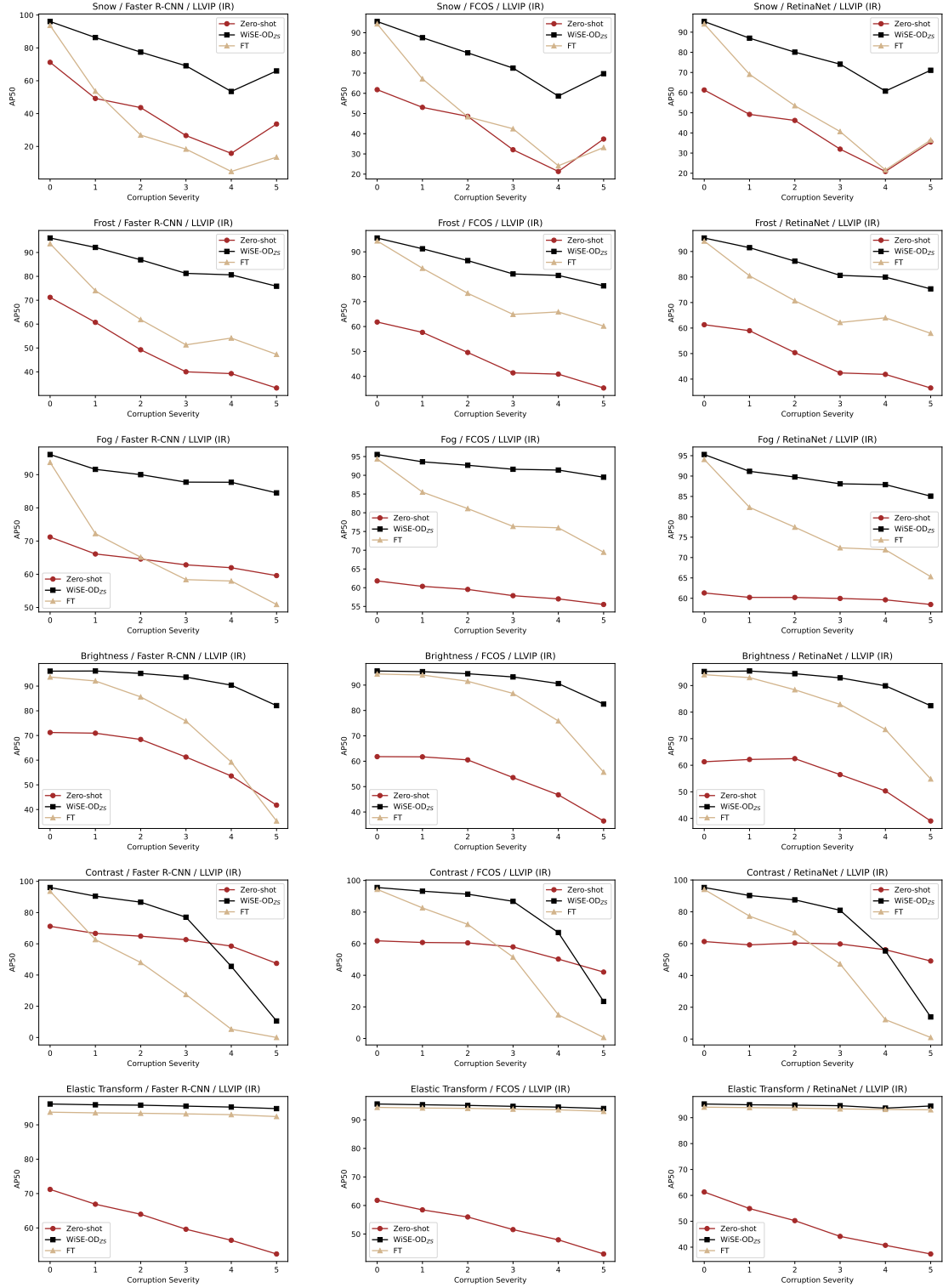


Figure 12. AP₅₀ performance for all detectors over different corruption severity levels for Snow, Frost, Fog, Brightness, Contrast, Elastic Transform. For each perturbation, we evaluated different levels of corruption for the Zero-Shot, WiSE-OD₂₅, and FT models for LLVIP-C.

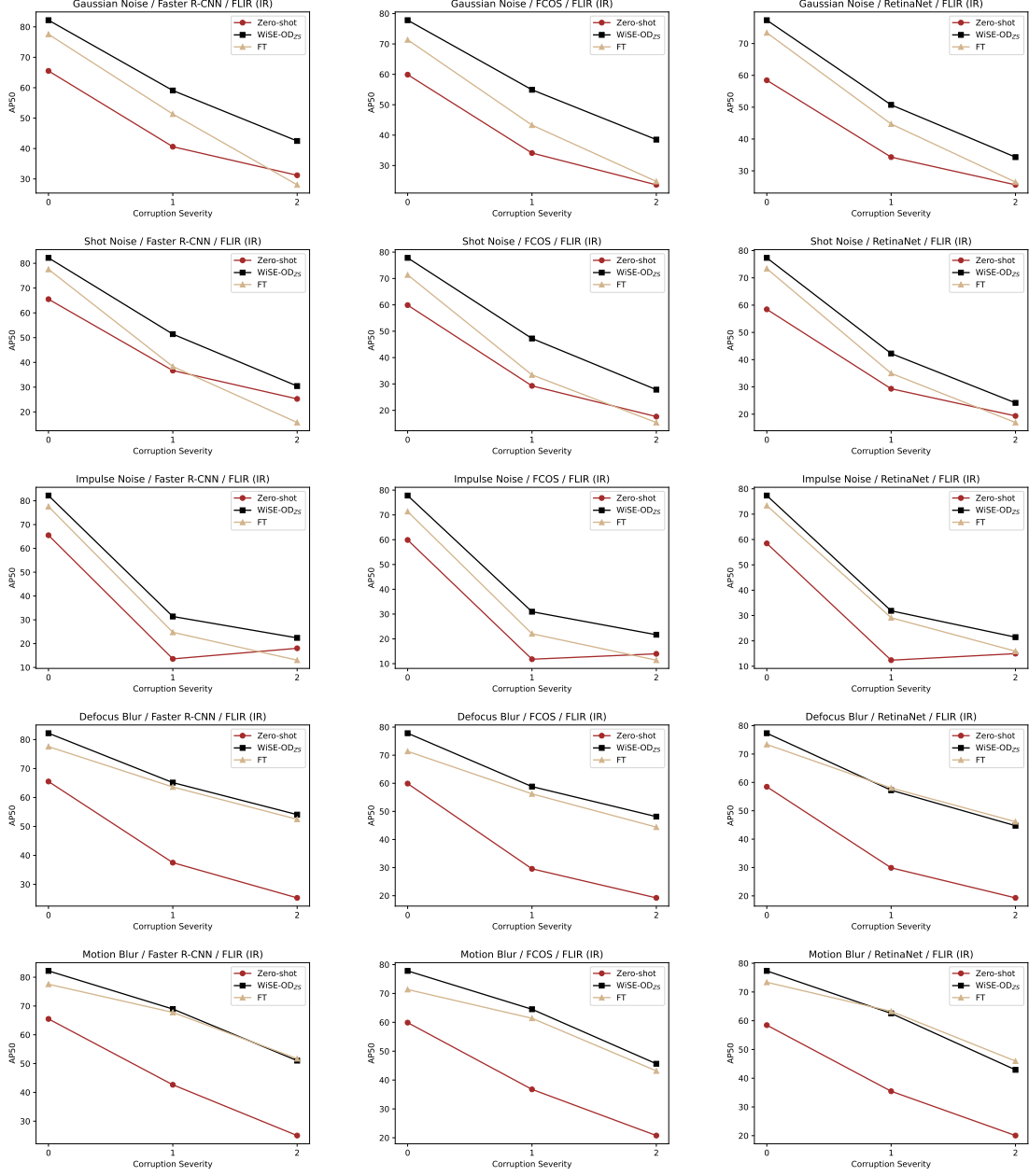


Figure 13. AP_{50} performance for all detectors over different corruption severity levels for Gaussian Noise, Shot Noise, Impulse Noise, Defocus Blur, Motion Blur. For each perturbation, we evaluated different levels of corruption for the Zero-Shot, WiSE-OD₂₅, and FT models for FLIR-C.

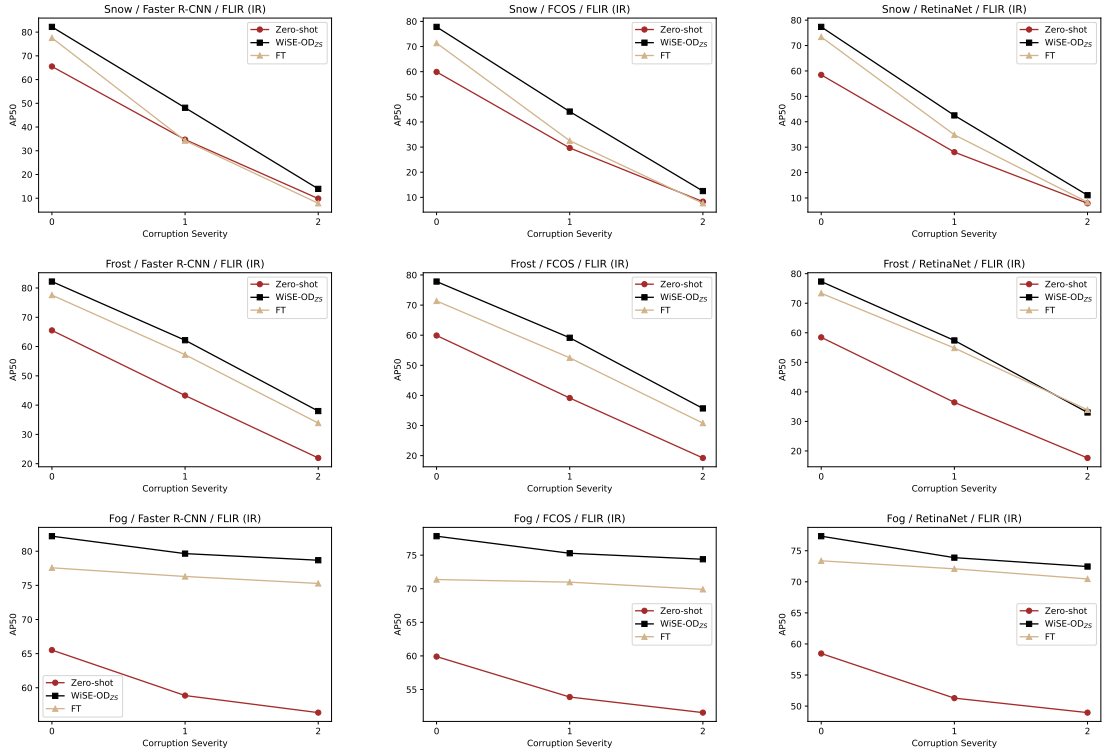


Figure 14. AP_{50} performance for all detectors over different corruption severity levels for Snow, Frost and Fog. For each perturbation, we evaluated different levels of corruption for the Zero-Shot, WiSE-OD₂₅, and FT models for FLIR-C.

References

- [1] Ayman Beghdadi, Malik Mallem, and Lotfi Beji. Benchmarking performance of object detection under image distortions in an uncontrolled environment. In *2022 IEEE International Conference on Image Processing (ICIP)*, pages 2071–2075. IEEE, 2022. [2](#)
- [2] Thomas Dubail, Fidel Alejandro Guerrero Peña, Heitor Rapela Medeiros, Masih Aminbeidokhti, Eric Granger, and Marco Pedersoli. Privacy-preserving person detection using low-resolution infrared cameras. In *European Conference on Computer Vision*, pages 689–702. Springer, 2022. [2](#)
- [3] Dan Hendrycks and Thomas Dietterich. Benchmarking neural network robustness to common corruptions and perturbations. In *International Conference on Learning Representations*, 2019. [2](#), [3](#), [8](#), [11](#), [12](#)
- [4] Pavel Izmailov, Dmitrii Podoprikin, Timur Garipov, Dmitry Vetrov, and Andrew Gordon Wilson. Averaging weights leads to wider optima and better generalization. *arXiv preprint arXiv:1803.05407*, 2018. [3](#)
- [5] Arthur Josi, Mahdi Alehdaghi, Rafael MO Cruz, and Eric Granger. Multimodal data augmentation for visual-infrared person reid with corrupted data. In *Proceedings of the IEEE/CVF Winter Conference on Applications of Computer Vision*, pages 32–41, 2023. [3](#)
- [6] Ananya Kumar, Aditi Raghunathan, Robbie Matthew Jones, Tengyu Ma, and Percy Liang. Fine-tuning can distort pre-trained features and underperform out-of-distribution. In *International Conference on Learning Representations*, 2022. [2](#), [3](#)
- [7] Tsung-Yi Lin, Michael Maire, Serge Belongie, James Hays, Pietro Perona, Deva Ramanan, Piotr Dollár, and C Lawrence Zitnick. Microsoft coco: Common objects in context. In *Computer Vision—ECCV 2014: 13th European Conference, Zurich, Switzerland, September 6–12, 2014, Proceedings, Part V 13*, pages 740–755. Springer, 2014. [2](#)
- [8] Tsung-Yi Lin, Priya Goyal, Ross Girshick, Kaiming He, and Piotr Dollár. Focal loss for dense object detection. In *Proceedings of the IEEE international conference on computer vision*, pages 2980–2988, 2017. [2](#)
- [9] Li Liu, Wanli Ouyang, Xiaogang Wang, Paul Fieguth, Jie Chen, Xinwang Liu, and Matti Pietikäinen. Deep learning for generic object detection: A survey. *International journal of computer vision*, 128:261–318, 2020. [2](#)
- [10] Xiaoqiong Liu, Yunhe Feng, Shu Hu, Xiaohui Yuan, and Heng Fan. Benchmarking the robustness of uav tracking against common corruptions. In *2024 IEEE 7th International Conference on Multimedia Information Processing and Retrieval (MIPR)*, pages 465–470. IEEE, 2024. [2](#)
- [11] Xiaofeng Mao, Yuefeng Chen, Yao Zhu, Da Chen, Hang Su, Rong Zhang, and Hui Xue. Coco-o: A benchmark for object detectors under natural distribution shifts. In *Proceedings of the IEEE/CVF International Conference on Computer Vision*, pages 6339–6350, 2023. [2](#)
- [12] Heitor Rapela Medeiros, Masih Aminbeidokhti, Fidel Alejandro Guerrero Peña, David Latortue, Eric Granger, and Marco Pedersoli. Modality translation for object detection

- adaptation without forgetting prior knowledge. In *European Conference on Computer Vision*, pages 51–68. Springer, 2024. 2
- [13] Heitor Rapela Medeiros, Fidel A Guerrero Pena, Masih Aminbeidokhti, Thomas Dubail, Eric Granger, and Marco Pedersoli. Hallucidet: Hallucinating rgb modality for person detection through privileged information. In *Proceedings of the IEEE/CVF Winter Conference on Applications of Computer Vision*, pages 1444–1453, 2024. 1
- [14] Heitor R Medeiros, Atif Belal, Srikanth Muralidharan, Eric Granger, and Marco Pedersoli. Visual modality prompt for adapting vision-language object detectors. *arXiv preprint arXiv:2412.00622*, 2025. 1, 2
- [15] Claudio Michaelis, Benjamin Mitzkus, Robert Geirhos, Evgenia Rusak, Oliver Bringmann, Alexander S Ecker, Matthias Bethge, and Wieland Brendel. Benchmarking robustness in object detection: Autonomous driving when winter is coming. *arXiv preprint arXiv:1907.07484*, 2019. 2, 4
- [16] Anitha Ramachandran and Arun Kumar Sangaiah. A review on object detection in unmanned aerial vehicle surveillance. *International Journal of Cognitive Computing in Engineering*, 2:215–228, 2021. 2
- [17] Shaoqing Ren, Kaiming He, Ross Girshick, and Jian Sun. Faster r-cnn: Towards real-time object detection with region proposal networks. *Advances in neural information processing systems*, 28:91–99, 2015. 2
- [18] Ramprasaath R Selvaraju, Michael Cogswell, Abhishek Das, Ramakrishna Vedantam, Devi Parikh, and Dhruv Batra. Grad-cam: Visual explanations from deep networks via gradient-based localization. In *Proceedings of the IEEE international conference on computer vision*, pages 618–626, 2017. 6
- [19] Michael Teutsch, Angel D Sappa, and Riad I Hammoud. Computer vision in the infrared spectrum: challenges and approaches. *Challenges and Approaches*, 2021. 1
- [20] Zhi Tian, Chunhua Shen, Hao Chen, and Tong He. Fcos: Fully convolutional one-stage object detection. In *Proceedings of the IEEE/CVF international conference on computer vision*, pages 9627–9636, 2019. 2
- [21] Mitchell Wortsman, Gabriel Ilharco, Samir Ya Gadre, Rebecca Roelofs, Raphael Gontijo-Lopes, Ari S Morcos, Hongseok Namkoong, Ali Farhadi, Yair Carmon, Simon Kornblith, et al. Model soups: averaging weights of multiple fine-tuned models improves accuracy without increasing inference time. In *International conference on machine learning*, pages 23965–23998. PMLR, 2022. 3
- [22] Mitchell Wortsman, Gabriel Ilharco, Jong Wook Kim, Mike Li, Simon Kornblith, Rebecca Roelofs, Raphael Gontijo Lopes, Hannaneh Hajishirzi, Ali Farhadi, Hongseok Namkoong, et al. Robust fine-tuning of zero-shot models. In *Proceedings of the IEEE/CVF conference on computer vision and pattern recognition*, pages 7959–7971, 2022. 2, 3
- [23] Aston Zhang, Zachary C Lipton, Mu Li, and Alexander J Smola. *Dive into deep learning*. Cambridge University Press, 2023. 2
- [24] Heng Zhang, Elisa Fromont, Sébastien Lefèvre, and Bruno Avignon. Multispectral fusion for object detection with cyclic fuse-and-refine blocks. In *2020 IEEE International Conference on Image Processing (ICIP)*, pages 276–280. IEEE, 2020. 4
- [25] Zhengxia Zou, Keyan Chen, Zhenwei Shi, Yuhong Guo, and Jieping Ye. Object detection in 20 years: A survey. *Proceedings of the IEEE*, 111(3):257–276, 2023. 1